

# Molecular insights into the interfacial tension of liquid sulfur with formation water/natural Gas: Effects of temperature, pressure, and composition



Zheng Li <sup>a,c,d</sup> , Daqian Zeng <sup>a,b</sup>, Tong Li <sup>a,b,\*</sup>, Qian Li <sup>a,b,\*\*</sup>, Rui Zhang <sup>a,b</sup>, Liang Huang <sup>c</sup>, Xiaoguang Wang <sup>c,d</sup>, Heng Wang <sup>c</sup>

<sup>a</sup> SINOPEC Key Laboratory of Marine Oil & Gas Reservoirs Production, Beijing, 102206, China

<sup>b</sup> SINOPEC Petroleum Exploration and Production Research Institute, Beijing, 102206, China

<sup>c</sup> State Key Laboratory of Oil and Gas Reservoir Geology and Exploitation, Chengdu University of Technology, Chengdu, 610059, China

<sup>d</sup> Tianfu Yongxing Laboratory, Chengdu, 610213, China

## ARTICLE INFO

### Keywords:

Interfacial tension  
Formation water  
Liquid sulfur  
Natural gas  
Molecular simulation

## ABSTRACT

The exploitation of natural gas with high H<sub>2</sub>S content may lead to the precipitation of dissolved sulfur. This process can negatively impact clean and sustainable production. The lack of reliable interfacial tension (IFT) data between liquid sulfur and formation water/natural gas makes it difficult to use numerical simulations for optimizing production strategies. This study develops and validates molecular models for liquid sulfur, natural gas, and formation water. These models accurately reproduce density, viscosity, and surface tension. Using molecular dynamics simulations, we calculate the IFTs between liquid sulfur and formation water/natural gas. We also investigate the effects of temperature (395–425 K), pressure (1–30 MPa), salinity (5000–200000 mg/L), ion type, and gas composition. The results demonstrate that liquid sulfur-formation water IFT > liquid sulfur surface tension > liquid sulfur-natural gas IFT. Increasing temperature and pressure decrease the IFTs, while ions significantly increase them. Liquid sulfur-brine IFTs follow the order: MgCl<sub>2</sub> > CaCl<sub>2</sub> > Na<sub>2</sub>SO<sub>4</sub> > NaHCO<sub>3</sub>. This is consistent with the strengths of ion-water interactions. H<sub>2</sub>S and CO<sub>2</sub> significantly reduce the liquid sulfur-natural gas IFT, with H<sub>2</sub>S exerting a more pronounced effect. When CO<sub>2</sub> and H<sub>2</sub>S coexist, H<sub>2</sub>S's IFT-reducing capacity is weakened due to competitive adsorption. This research provides critical parametric inputs for numerical simulations to control sulfur precipitation and enhance recovery in high-H<sub>2</sub>S gas reservoirs.

## 1. Introduction

Natural gas offers environmental benefits over coal and oil, making it increasingly important for global energy production (Kotagodahetti et al., 2023). High H<sub>2</sub>S-content natural gas reservoirs hold significant resource potential and are key to improving natural gas system production (Liu et al., 2010). In high-H<sub>2</sub>S gas reservoirs, formation pressure decreases during development. This reduces natural gas's ability to dissolve sulfur, leading to sulfur precipitation, migration, and sedimentation (Castro et al., 2023; Li et al., 2024). At reservoir depths over 5000 m, temperatures exceed sulfur's melting point of 393 K (Meyer, 1976), causing sulfur to become liquid. This results in multiphase flow involving liquid sulfur, natural gas, and formation water (Coşkuner,

1994).

Interfacial tension (IFT) results from imbalanced interfacial forces and causes liquid surface contraction (Berry et al., 2015; Cai et al., 2021). It is critical for multiphase flow behavior and distribution in porous media (Cai et al., 2025; Cao et al., 2024; Xu et al., 2020). Extensive research has been conducted on gas-water IFT using pendant drop and bubble rise methods (Kharazi et al., 2023; Zhang and Wang, 2023). CH<sub>4</sub>, the primary component of natural gas, exhibits IFT with water (IFT<sub>CH4-water</sub>) that decreases with increasing temperature and pressure, while increasing with higher salinity (Kashefi et al., 2016; Yasuda et al., 2016).

CO<sub>2</sub> and H<sub>2</sub>S are the primary sour components in high-H<sub>2</sub>S natural gas. Typically, the IFT between CO<sub>2</sub> and water (IFT<sub>CO2-water</sub>) decrease

\* Corresponding author. SINOPEC Key Laboratory of Marine Oil & Gas Reservoirs Production, Beijing, 102206, China.

\*\* Corresponding author. SINOPEC Key Laboratory of Marine Oil & Gas Reservoirs Production, Beijing, 102206, China.

E-mail addresses: [lit95944.syky@sinopec.com](mailto:lit95944.syky@sinopec.com) (T. Li), [liqian2022.syky@sinopec.com](mailto:liqian2022.syky@sinopec.com) (Q. Li).

significantly with higher pressure but increases linearly with salinity (Zhang and Wang, 2023). As pressure approaches the stabilization point, IFT<sub>CO<sub>2</sub>-water</sub> ultimately reaches an asymptotic value (plateau) (Aggelopoulos et al., 2010). The valence of cations positively correlates with an increase in IFT<sub>CO<sub>2</sub>-water</sub> (Chen et al., 2017). One study found little change in IFT<sub>CO<sub>2</sub>-water</sub> with salinity, possibly because the salt concentration used was low (Chiquet et al., 2007). The temperature dependence of IFT<sub>CO<sub>2</sub>-water</sub> is complex, with studies reporting increases (Li et al., 2012; Liu et al., 2017), decreases (Chiquet et al., 2007; Saraji et al., 2014), unchanged (Chi et al., 2022) or nonmonotonic behaviors (Bachu and Bennion, 2009). This variability can be attributed to CO<sub>2</sub> phase changes and its solubility in water under diverse temperature and pressure conditions (Mutailipu et al., 2019; Zhang and Wang, 2023). IFT<sub>CO<sub>2</sub>-water</sub> is lower than IFT<sub>CH<sub>4</sub>-water</sub>, and adding CO<sub>2</sub> to CH<sub>4</sub> further reduces IFT<sub>CH<sub>4</sub>-water</sub> (Liu et al., 2016; Ren et al., 2000).

In contrast to IFT<sub>CO<sub>2</sub>-water</sub>, experimental data on the IFT between H<sub>2</sub>S and water (IFT<sub>H<sub>2</sub>S-water</sub>) are limited. Shah et al. (2008) made the first systematic measurements of IFT<sub>H<sub>2</sub>S-water</sub> under geological conditions. They found that IFT<sub>H<sub>2</sub>S-water</sub> decreased with pressure until reaching saturation pressure, after which it stabilized. This behavior is analogous to the pressure-dependent changes in IFT<sub>CO<sub>2</sub>-water</sub> (Aggelopoulos et al., 2010). Notably, IFT<sub>H<sub>2</sub>S-water</sub> is about 30–40 % of IFT<sub>CO<sub>2</sub>-water</sub> and 20 % of IFT<sub>CH<sub>4</sub>-water</sub> under similar temperature and pressure conditions (Shah et al., 2008).

Data on IFT between liquid sulfur and water (IFT<sub>sulfur-water</sub>) are similarly scarce. Fanelli (1950) and Ono and Matsushima (1957) investigated the surface tension of sulfur within a temperature range of 393–708 K, observing a decrease with increasing temperature. Fanelli (1950) found that adding water did not affect sulfur's surface tension at 396 K. In a subsequent study, Matsushima and Ono (1958) measured IFT<sub>sulfur-water</sub> between 383 and 453 K. They found a negative linear relationship between IFT<sub>sulfur-water</sub> and temperature, with a notable turning point at 433 K.

Experimental measurement of IFT involving liquid sulfur and H<sub>2</sub>S is extremely challenging due to the high melting point of sulfur (393 K) (Meyer, 1976) and the toxicity of H<sub>2</sub>S (Zhang et al., 2014). Maintaining temperatures above sulfur's melting point is necessary to prevent condensation and pipeline blockages, which complicates experimental setups. Additionally, the toxicity of H<sub>2</sub>S poses significant risks, including challenges in tail gas management. Its high solubility in water can lead to corrosive conditions (Gong et al., 2023), and the high pressures required for high-H<sub>2</sub>S in-situ conditions further exacerbate safety and operational difficulties.

Molecular dynamics (MD) simulations offer an alternative approach for investigating IFT in multiphase fluid systems, overcoming experimental limitations associated with extreme temperature and pressure ranges (Hayatizadeh et al., 2024; Mim et al., 2025; Zhang et al., 2024), as well as challenges posed by toxic gases such as H<sub>2</sub>S (Qian et al., 2024). MD simulations are important because they allow molecular-scale study of interfacial phenomena, offering details that experiments cannot easily provide (Dong et al., 2023; Fan et al., 2024; Huang et al., 2024; Lu et al., 2023; Xia et al., 2024).

Dehaghani et al. (2023) used MD simulations to predict IFT<sub>H<sub>2</sub>S-water</sub>, with an average absolute deviation of 4.93 % from experimental data. They found that IFT<sub>H<sub>2</sub>S-water</sub> decreased under higher pressure but increased with higher temperature and salinity. The varying effects of different salts on IFT<sub>H<sub>2</sub>S-water</sub> were attributed to cation distribution in the aqueous phase and water molecule structure near the interface. Ofori et al. (2023) studied interfacial properties between acid gas (a mixture of CO<sub>2</sub> and H<sub>2</sub>S) and water under reservoir-like conditions. Despite overestimating IFT values, their simulations demonstrated trends consistent with experimental observations as pressure increased. Through analysis of density distributions and radial distribution functions, they determined interface thickness and concluded that CO<sub>2</sub> dominated the interfacial interactions with water. González-Barramúno et al. (2024) examined thermodynamic properties of the acid gas-water

interface, observing H<sub>2</sub>S phase changes that elucidated IFT variations with pressure. For multiphase systems involving liquid sulfur, MD simulations have been utilized to calculate sulfur solubility (Li et al., 2024; Wei et al., 2022, 2023).

Despite significant advancements in measuring and calculating IFT, the IFT between liquid sulfur and formation water/natural gas remains unexplored, both experimentally or computationally. This gap is particularly evident when considering the effects of temperature, pressure, and the composition of formation water and natural gas. To address this lack of data in this work, we establish and validate molecular models for liquid sulfur, natural gas, and formation water as a foundation for MD simulations of these systems. Using these validated models, we perform MD simulations to investigate the variations in IFT for liquid sulfur-formation water and liquid sulfur-natural gas under in-situ conditions.

## 2. Models and methods

This section presents the molecular models and their associated force fields. It also outlines the simulation protocols and post-processing analytical methods employed in this study.

### 2.1. Molecular models and force fields

We focus on the interactions between natural gas, formation water, and liquid-phase condensate sulfur in high-H<sub>2</sub>S natural gas reservoirs. Table A1 and Figure A1 provide the compositional analysis of natural gas and formation water, respectively. These data are from a representative high-H<sub>2</sub>S natural gas field in the Sichuan Basin. The formation water analysis includes 103 samples. The natural gas is primarily composed of CH<sub>4</sub>, with significant amounts of H<sub>2</sub>S and CO<sub>2</sub> (Ma et al., 2008). The formation water typically contains salts such as CaCl<sub>2</sub>, MgCl<sub>2</sub>, Na<sub>2</sub>SO<sub>4</sub> and NaHCO<sub>3</sub>.

Sulfur exists in various allotropes, with the octatomic ring (S<sub>8</sub>) being the fundamental unit. Previous studies have shown that liquid sulfur is predominantly composed of S<sub>8</sub> rings (Ludwig et al., 2002; Steudel et al., 1985). Therefore, our study incorporates molecules including CH<sub>4</sub>, H<sub>2</sub>S, CO<sub>2</sub>, H<sub>2</sub>O, and S<sub>8</sub>, as well as ions such as Ca, Mg, Na, Cl, HCO<sub>3</sub> and SO<sub>4</sub>. These components are illustrated in Fig. 1.

All atoms in these molecules and ions are explicitly modeled. Non-bonded interactions comprise van der Waals ( $E_{vdW}$ ) and electrostatic ( $E_{Coul}$ ) forces. They are calculated using the Lennard-Jones 12-6 (LJ 12-6, Equation (1)) and Coulombic (Equation (2)) potential functions, respectively. The LJ parameters for heterogeneous particle interactions are determined using the Waldman-Hagler mixing rules (Waldman and Hagler, 1993) (Equations (3a) and (3b)). Bonded potentials encompass bond ( $E_{bond}$ ), angle ( $E_{angle}$ ), and dihedral ( $E_{dihedral}$ ) interactions, described by Equations (4)–(6), respectively. Equations (5b) and (6) are specially applies to S<sub>8</sub> molecules.

$$E_{vdW} = 4e_{ij} \left[ \left( \frac{\sigma_{ij}}{r_{ij}} \right)^{12} - \left( \frac{\sigma_{ij}}{r_{ij}} \right)^6 \right], r_{ij} < r_c \quad (1)$$

$$E_{Coul} = \frac{q_i q_j}{4\pi\epsilon_0 r_{ij}}, r_{ij} < r_c \quad (2)$$

$$\epsilon_{ij} = \frac{2\sqrt{\epsilon_i \epsilon_j} \sigma_i^3 \sigma_j^3}{\sigma_i^6 + \sigma_j^6} \quad (3a)$$

$$\sigma_{ij} = \left( \frac{1}{2} \left( \sigma_i^6 + \sigma_j^6 \right) \right)^{\frac{1}{6}} \quad (3b)$$

$$E_{bond} = K_b (r - r_0)^2 \quad (4)$$

$$E_{angle} = K_a (\theta - \theta_0)^2 \quad (5a)$$

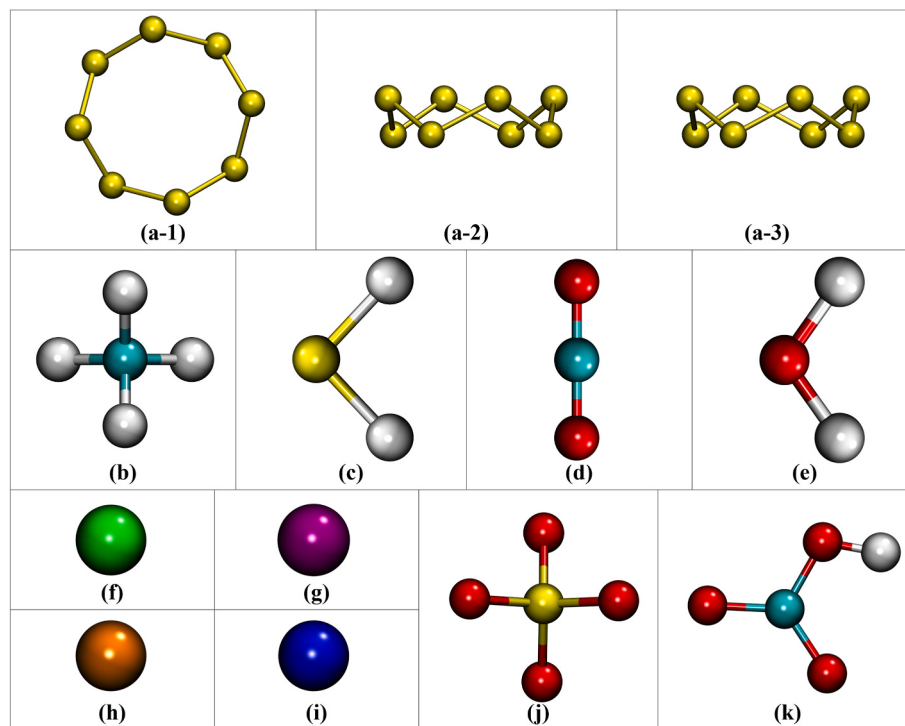


**Fig. 1.** Molecular models of (a-1) top, (a-2) front, and (a-3) side views of S<sub>8</sub>; (b) CH<sub>4</sub>; (c) H<sub>2</sub>S; (d) CO<sub>2</sub>; (e) H<sub>2</sub>O; (f) Ca cation; (g) Mg cation; (h) Na cation; (i) Cl anion; (j) SO<sub>4</sub> anion; (k) HCO<sub>3</sub> anion. Color code for atoms: cyan, carbon; white, hydrogen; yellow, sulfur; red, oxygen; green, calcium; purple, magnesium; orange, sodium; blue, chlorine. (For interpretation of the references to colour in this figure legend, the reader is referred to the Web version of this article.)

$$E_{\text{angle}} = K_a [\cos(\theta) - \cos(\theta_0)]^2 \quad (5b)$$

$$E_{\text{dihedral}} = \sum_{n=1}^5 A_n \cos^{n-1}(\phi) \quad (6)$$

In these equations,  $r_{ij}$  (Å) denotes the interatomic distance between atoms  $i$  and  $j$ , with  $r_c$  as the cut-off distance.  $\epsilon$  (kcal/mol) and  $\sigma$  (Å) represent the LJ potential well depth and zero-potential distance, respectively.  $q$  denotes the atomic charge.  $K_b$  (kcal/Å<sup>2</sup>),  $K_a$  (kcal/rad<sup>2</sup>), and  $A_n$  (kcal) correspond to bond, angle and dihedral force constants, respectively.  $r$  and  $r_0$  (both in Å) represent the bond length and the equilibrium bond length, respectively.  $\theta$  and  $\theta_0$  (both in degrees) represent the angle and the equilibrium angle, respectively.  $\phi$  (in degrees) represents the dihedral angle.

CH<sub>4</sub> molecules are modeled with the OPLS-AA force fields (Jorgensen et al., 1996), while CO<sub>2</sub> molecules utilize the TraPPE force field (Potoff and Siepmann, 2001). H<sub>2</sub>O molecules use the SPC/E model (Berendsen et al., 1987). For H<sub>2</sub>S molecules, the force field parameters from Nath (2003) are employed. Ca and Cl ions are described using the Clayff force field (Cyan et al., 2021), while Mg ions use the OPLS-AA force field (Jorgensen et al., 1996). The combination of Clayff and OPLS-AA force fields is implemented in the msi2lmp tool in LAMMPS (Thompson et al., 2022). The force field parameters for NaHCO<sub>3</sub> are based on the work of Yin et al. (2023) and Zeebe (2011), while those for Na<sub>2</sub>SO<sub>4</sub> are derived from Mamatkulov et al. (2018). HCO<sub>3</sub> and SO<sub>4</sub> ions are treated as rigid bodies without bonded interactions. S<sub>8</sub> molecules are modeled using the force field developed by Ballone and Jones (2003), which was parametrized by fitting the equilibrium structure and vibrational frequencies of S<sub>8</sub> obtained from density functional theory calculations. This force field has been validated for a broad temperature range, encompassing the melting point of sulfur up to its phase transition temperature of 432 K (Jones and Ballone, 2003). Furthermore, it has been successfully employed to calculate S<sub>8</sub> solubility under high temperature and high pressure conditions (Li et al., 2024). Detailed

parameters are provided in Tables A2-A7 of the supporting information. These force field parameters have been validated through density and viscosity calculations, with comparisons presented in Figures A2-A7. Additionally, surface tension calculations serve as another validation method, as demonstrated in Section 3.1.

The simulations for molecules other than H<sub>2</sub>O and S<sub>8</sub> align well with reference data. The deviations are observed for both water and liquid sulfur due to distinct reasons. For H<sub>2</sub>O, The SPC/E model uses constrained bonds and angles to enhance computational efficiency (Berendsen et al., 1987), which introduces relatively larger deviations in simulated density compared to the reference (Figure A5). In the case of liquid sulfur, the deviations arise from two primary factors. First, modeling liquid sulfur accurately is inherently challenging due to its complex structure and temperature-dependent transitions (Ludwig et al., 2002). Liquid sulfur consists of various molecular species, including S<sub>6</sub>, S<sub>7</sub>, and S<sub>n</sub> ( $n > 8$ ), as well as reactive intermediates, all of which influence its properties. While S<sub>8</sub> dominates below the polymerization temperature (432 K), experimental studies indicate the presence of other species that significantly affect its behavior (Steudel et al., 1985). Additionally, impurities or compositions in experimental samples, such as organic matter, SO<sub>2</sub>, or H<sub>2</sub>S, can strongly impact the viscosity of liquid sulfur (Bacon and Fanelli, 1943), further complicating comparisons. In our simulations, pure S<sub>8</sub> molecules are used as the representative form of liquid sulfur, which simplifies the system but introduces deviations relative to experimental data. Second, viscosities derived from molecular simulations are inherently sensitive to factors such as force fields, cutoff radius, dielectric constant, and the treatment of long-range interactions, which influence accuracy (Hess, 2002). As a result, some degree of deviation is expected when comparing simulation results to experimental measurements (Figures A6 and A7).

## 2.2. Simulation and calculation methods

The bulk density calculation follows a straightforward procedure. A specified number of CH<sub>4</sub>, H<sub>2</sub>S, CO<sub>2</sub>, H<sub>2</sub>O or S<sub>8</sub> molecules are randomly

inserted into a  $20 \times 20 \times 20 \text{ \AA}^3$  simulation box. This setup is followed by energy minimization. Next, we perform a 0.5-ns canonical ensemble (NVT) simulation, followed by a 2.0-ns isothermal-isobaric ensemble (NPT) simulation. Once the system reaches the desired temperature and pressure, a 1.0-ns production simulation is performed. The density  $\rho$  ( $\text{g}/\text{cm}^3$ ) is calculated as:

$$\rho = \frac{n \times M}{V \times N_A} \quad (7)$$

where  $n$ ,  $N_A$  ( $\text{mol}^{-1}$ ),  $M$  ( $\text{g/mol}$ ) and  $V$  ( $\text{cm}^3$ ) are the molecule number, the Avogadro constant, the molar mass and the equilibrium volume, respectively.

The radial distribution function (RDF) calculation involves dividing the space around a central atom into a series of concentric shells. Let  $r_i$  represent the distance from the central atom to the  $i$ th shell,  $\rho(r_i)$  be the density within the  $i$ th shell, and  $\rho$  be the bulk density. The RDF can be calculated as:

$$g(r_i) = \frac{\langle \rho(r_i) \rangle}{\rho} \quad (8)$$

To calculate the density distribution, the space along the  $x$ -direction is divided into a series of bins. Let  $W_x$  be the width of each bin,  $x_i$  the  $x$ -coordinate of the volume centroid in the  $i$ th bin, and  $N(i, T)$  the number of molecules in that bin at step  $T$ . The number density  $\rho_{\text{number}}$  and mass density  $\rho_{\text{mass}}$  can then be calculated as:

$$\rho_{\text{number}}(x_i) = \sum_{T=T_S}^{T_E} \frac{N(i, T)}{(T_E - T_S + 1) \times L_y \times L_z \times W_x} \quad (9)$$

$$\rho_{\text{mass}} = \frac{\rho_{\text{number}}}{N_A} \times M \quad (10)$$

where  $T_S$  and  $T_E$  are the initial and end timesteps for data analysis, respectively;  $M$  is the molar mass.

The viscosity is calculated using non-equilibrium MD simulations. A shear force  $\tau_{xz}$  (Pa) is applied to the  $\text{H}_2\text{O}$  or  $\text{S}_8$  simulation system, which is kept at a constant temperature and pressure. This creates a shear flow, leading to a stable velocity distribution  $u_x$  (m/s) along the  $z$ -axis once equilibrium is reached (Figure A8). According to Newton's law of viscosity, the viscosity of  $\text{H}_2\text{O}$  or  $\text{S}_8$  can be calculated as:

$$\mu = \frac{\tau_{xz}}{du_x/dz} \quad (11)$$

The surface tension is calculated using the method by Yuet and Blankschtein (2010). Initially, a sufficient number of molecules are randomly inserted into a simulation box to achieve equilibrium dimensions of  $L_x = L_y = L_z \approx 5 \text{ nm}$  after performing energy minimization, NVT and NPT simulations. The periodic boundary in the  $x$ -direction is then removed, allowing the simulation box to expand in that direction, resulting in  $L_y = L_z = L_x/\alpha$ , where  $3 < \alpha < 7$ . An NVT simulation is then performed on the enlarged simulation box and the pressure tensors  $p_{xx}$ ,  $p_{yy}$  and  $p_{zz}$  (Pa) are recorded. The surface tension  $\gamma_s$  (N/m) is calculated as:

$$\gamma_s = \frac{1}{2} L_x \left( p_{xx} - \frac{1}{2} (p_{yy} + p_{zz}) \right) \quad (12)$$

The interfacial tension ( $\gamma_i$ ) calculation is based on the simulation system depicted in Fig. 2.  $\text{S}_8$  molecules occupy the central region, while formation water ( $\text{H}_2\text{O}$  and ions) or natural gas ( $\text{CH}_4$ ,  $\text{H}_2\text{S}$  and  $\text{CO}_2$ ) molecules are positioned in the bilateral regions. This is followed by energy minimization and a simulated annealing process, which consists of a series of NVT and NP<sub>xx</sub>T simulations (Table 1). The subscript xx indicates that only the pressure in the  $x$ -direction is controlled.

Initially, the two-phase system is relaxed at 425 K in an NVT ensemble for 0.1 ns. This elevated temperature provides significant kinetic energy to the system, ensuring thorough relaxation. The

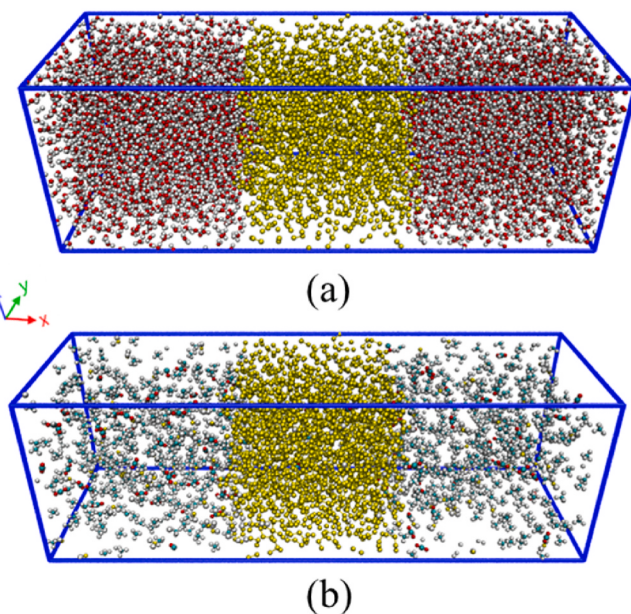


**Fig. 2.** Molecular simulation system for interfacial tension calculation: (a) liquid sulfur-formation water and (b) liquid sulfur-natural gas.

**Table 1**  
Molecular simulation process for interfacial tension calculation.

| Stage | Ensemble           | Temperature/K             | Pressure/MPa        | Timestep/fs | Time/ns |
|-------|--------------------|---------------------------|---------------------|-------------|---------|
| 1     | NVT                | 425                       | –                   | 0.1         | 0.1     |
| 2     | NVT                | 425 → $T_{\text{target}}$ | –                   | 0.1         | 0.1     |
| 3     | NVT                | $T_{\text{target}}$       | –                   | 1.0         | 1.0     |
| 4     | NP <sub>xx</sub> T | $T_{\text{target}}$       | $P_{\text{target}}$ | 1.0         | 5.0     |
| 5     | NVT                | $T_{\text{target}}$       | –                   | 1.0         | 30.0    |

temperature is then gradually decreased to the target temperature  $T_{\text{target}}$  over 0.1 ns, followed by a 1.0-ns NVT simulation at  $T_{\text{target}}$ . Once the system temperature stabilizes, an NP<sub>xx</sub>T simulation is performed by applying pressure in the  $x$ -direction. After 5.0 ns, both the temperature and the pressure in the  $x$ -direction reach equilibrium. Figure A9 illustrates the changes in temperature and pressure over the simulation time for  $T_{\text{target}} = 405 \text{ K}$ ,  $P_{\text{target}} = 30 \text{ MPa}$ .  $T_{\text{target}}$  and  $P_{\text{target}}$  in this work are selected based on the phase diagram of sulfur (Ferreira and Lobo, 2011), as shown in Figure A10, to ensure that  $\text{S}_8$  remains in liquid phase.

To maintain molecular integrity at the boundary, the periodic boundary in the  $x$ -direction is removed.  $L_x$  is manually adjusted to the  $L_x$ -average, representing the mean length of the system in the  $x$ -direction during the final 2.0-ns NP<sub>xx</sub>T simulation. Finally, an additional 30.0-ns NVT simulation is conducted. Trajectories and pressure tensors from the last 10.0 ns are collected for interfacial tension calculation using Equation (12).

To ensure statistical reliability, three independent simulations with different initial coordinates and velocities are performed for calculating interfacial tension, as well as density, viscosity, and surface tension.

### 3. Results and discussion

#### 3.1. Surface tension

First, we calculate the surface tensions of water and liquid sulfur and compare them with reference data shown in Fig. 3. As the temperature increases, surface tension generally decreases due to the heightened kinetic activity of liquid molecules, which weakens the cohesive forces at the liquid surface. Within the simulation temperature range, the surface tension of water decreases from 57.18 mN/m to 32.19 mN/m as

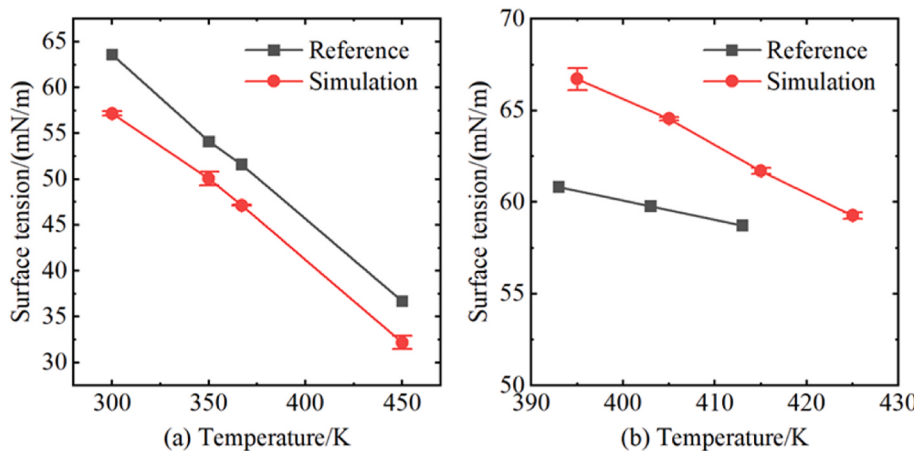


Fig. 3. Surface tension variation with temperature for (a) water and (b) liquid sulfur.

the temperature rises from 300 K to 450 K. In contrast, the surface tension of liquid sulfur decreases from 66.71 mN/m to 59.26 mN/m as the temperature increases from 395 K to 425 K.

Compared to the reference surface tension of water (Vega and de Miguel, 2007), our simulation results are lower, likely due to constraints on the bonds and angles of water molecules in the simulation. In contrast, the simulated surface tension of liquid sulfur is higher than the reference value (Fanelli, 1950), potentially because pure S<sub>8</sub> molecules are used to represent liquid sulfur. Deviations in surface tension are also influenced by several well-documented factors, including finite size effects, interaction range, truncation effects, the choice of mechanical or thermodynamic definitions, and the application of long-range corrections (Ghoufi and Malfreyt, 2018). For instance, the SPC/E water model achieves average deviations below 5 % from experimental values over the 328–573 K range, but deviations can exceed 25 % depending on methodology (Alejandre et al., 1995). Similarly, Werth et al. (2017) reported deviations ranging from 2 % to 62 % (average ~20 %), for 33 real fluids. Within this context, the deviations in our results (5.0 %–12.3 %) for both water and liquid sulfur are consistent with prior findings. Additionally, our simulated trends align with reference data as temperature increases.

The deviations observed can potentially influence the interfacial tension calculations (Berry et al., 2015). For water, simulations tend to underestimate densities and surface tensions compared to experimental reference data, indicating an underestimation of intermolecular forces and surface energy. Conversely, for liquid sulfur, simulations yield higher viscosities, densities, and surface tensions relative to experimental data, suggesting an overestimation of intermolecular forces and surface energy. According to the Good-Girifalco equation (Girifalco and Good, 1957),  $\gamma_{1,2} = \gamma_1 + \gamma_2 - W_{1,2}$ , where  $\gamma_{1,2}$  is the interfacial energy,  $\gamma_1$  and  $\gamma_2$  are the surface energies of the phases, and  $W_{1,2}$  is the adhesion energy between them. In our simulations, the deviations in surface energies of the two phases could offset each other to some extent, particularly if the molecular mixing rules accurately capture the interactions between the two phases. However, it is important to note that the accuracy of these predictions is contingent on how well the intra-phase interactions are modeled in the simulation. Uncertainties in  $\gamma_1$  and  $\gamma_2$  may propagate to  $W_{1,2}$ , thereby introducing an additional layer of uncertainty to the calculated interfacial tension values.

### 3.2. Liquid sulfur-formation water interfacial tension

Upon the precipitation of liquid sulfur, two-phase contact may occur between liquid sulfur and formation water, as well as between liquid sulfur and natural gas. We begin by calculating the interfacial tension between liquid sulfur and formation water, investigating the influences

of temperature, pressure, formation water salinity, and ion type. Subsequently, we analyze the interfacial structures to elucidate the observed variations in interfacial tension. The dissolution of H<sub>2</sub>S and CO<sub>2</sub> in formation water, along with any associated chemical reactions, is not considered in this study.

#### 3.2.1. Temperature effects

Based on the formation water analysis presented in Figure A1, CaCl<sub>2</sub> solution with salinity below 50000 mg/L is the most prevalent brine. Consequently, we employ pure water and a 50000 mg/L CaCl<sub>2</sub> solution to represent formation water. At a constant pressure of 30 MPa, we investigate the temperature effects on the liquid sulfur-formation water interfacial tension at 395 K, 405 K, 415 K and 425 K, as illustrated in Fig. 4.

The observed interfacial tensions exceed the surface tensions of both water and liquid sulfur. This phenomenon arises from the differing molecular interactions in each phase. Water molecules, being highly polar, form strong hydrogen bonds that result in high cohesive forces (Li

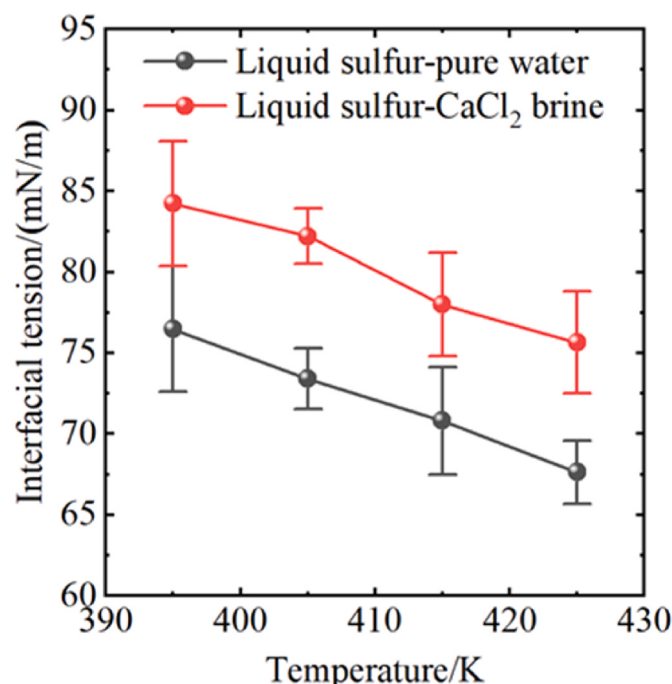


Fig. 4. Temperature effects on liquid sulfur – formation water interfacial tension.

et al., 2019). In contrast,  $S_8$  molecules, while less polar than water, exhibit significant intermolecular interactions due to vdW forces (Table A7). This considerable disparity in these molecular interactions creates weak adhesive forces between the phases, generating a high-energy interface.

As the temperature increases, the liquid sulfur-formation water interfacial tension decreases. Moreover, the interfacial tension between liquid sulfur and  $\text{CaCl}_2$  brine exceeds that between liquid sulfur and pure water.

To better understand these changes in interfacial tension, we analyze the molecular structure across the interface by calculating density distributions, as illustrated in Fig. 5. The simulations are conducted at 395 K and 30 MPa.

The density profiles exhibit plateaus in both water and sulfur phases. The average plateau values of 1.91 g/ml for sulfur and 0.95 g/ml for water, which closely match the simulated bulk densities of liquid sulfur (1.90 g/ml) and water (0.94 g/ml). Progressing from the water phase to the sulfur phase, the water density decreases from its plateau to zero, while the liquid sulfur density does the opposite. Notably, these density transitions are gradual, indicating a finite thickness of the two-phase interface.

To define this interfacial region, we employ the “10–90” criterion (Xu et al., 2022), which measures from 10 % to 90 % of the bulk density on the liquid sulfur density distribution curve (Fig. 5a). This method enables quantification of the interface thickness.

Fig. 6 shows the temperature-dependent increase in interface thickness for liquid sulfur-pure water and liquid sulfur- $\text{CaCl}_2$  brine systems. The interfacial width arises from molecular penetrations driven by thermal fluctuations (Culcer et al., 2010; Rao and Lee, 2003) and significantly influences mass transfer (Das and Ali, 2019). As temperature rises, the densities of water and liquid sulfur decrease (Figures A5 and A6), weakening the cohesive forces within the bulk phases (Fan et al., 2020). This reduction in molecular attraction at the interface promotes greater molecular exchange between the two phases, enhancing miscibility. The trend indicates that higher temperatures increase miscibility between liquid sulfur and formation water due to intensified molecular motion and the disruption of interfacial structures. Interfacial tension arises from unbalanced interaction forces between molecules at the interface. As the two phases become more miscible, the force imbalance diminishes, leading to a reduction in interfacial tension.

The interface thickness of liquid sulfur- $\text{CaCl}_2$  brine is consistently thinner, indicating a higher interfacial tension (Fig. 4). To further understand this phenomenon, we analyze the density distribution of Ca and Cl ions across the interface (Fig. 5b). These ions are primarily found in the bulk water rather than at the interface. Their strong interactions with water molecules, as detailed in Section 3.2.4, contribute to the force imbalance at the interface, increasing interfacial tension. In contrast to surfactants, which accumulate at the interface and reduce

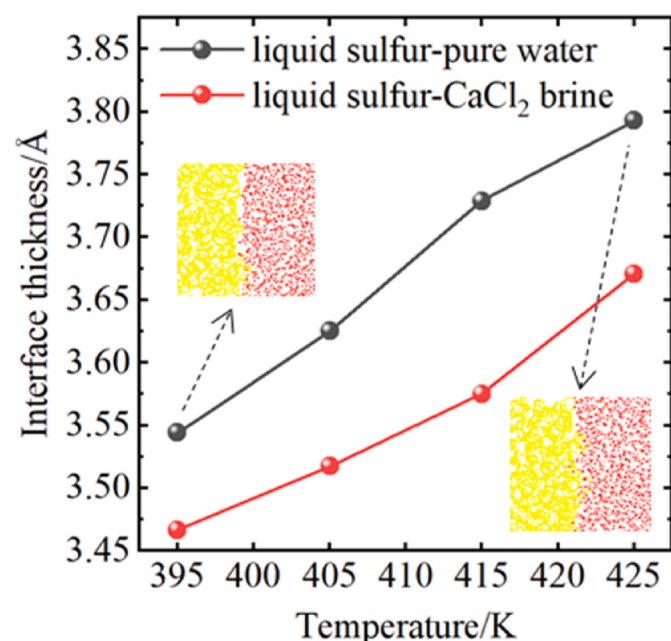


**Fig. 6.** Temperature effects on the thickness of liquid sulfur – formation water interface. The insets are the corresponding molecular snapshots at the interface.

interfacial tension (Yarveicy, 2023), Ca and Cl ions increase interfacial tension and tend to distribute preferentially in the bulk water. This distribution pattern aligns with the findings presented in Figs. 4 and 6.

### 3.2.2. Pressure effects

We then maintain the temperature at 405 K while varying the pressure to calculate interfacial tension at 1 MPa, 10 MPa, 20 MPa and 30 MPa (Fig. 7a). Results indicate that interfacial tension decreases as pressure increases. Moreover, the interfacial tension of the liquid sulfur- $\text{CaCl}_2$  brine remains consistently higher across all pressure conditions.

We calculate the interface thickness to elucidate changes in interfacial tension, as illustrated in Fig. 7b. While cohesive forces within the bulk phase increase with pressure, higher pressure also enhances interactions between the two phases at the interface (da Rocha et al., 2001). At elevated pressures, the interface between liquid sulfur and water deforms, as depicted in the inset, indicating increased miscibility between liquid sulfur and formation water due to the disruption of interfacial structures. This disruption reduces the force imbalance at the interface, leading to a decrease in interfacial tension. Comparing Fig. 7 with Figs. 4 and 6 reveals that, within the simulation range, temperature exerts a greater influence on interface thickness than pressure.

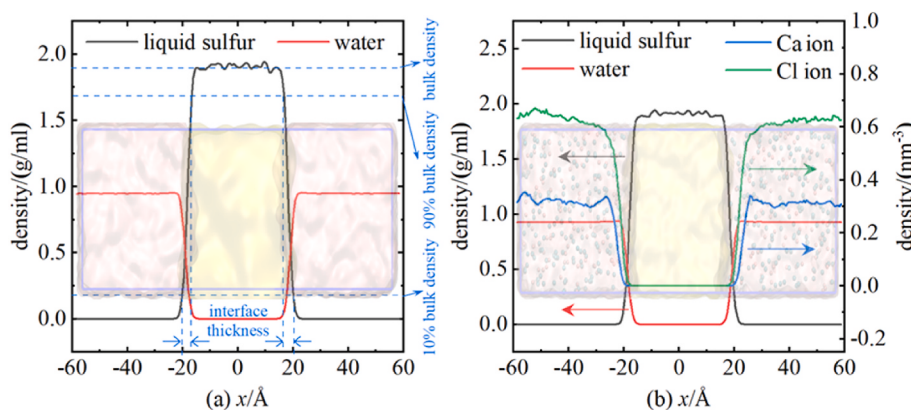


**Fig. 5.** Density distribution of (a) liquid sulfur – pure water and (b) liquid sulfur –  $\text{CaCl}_2$  brine systems.

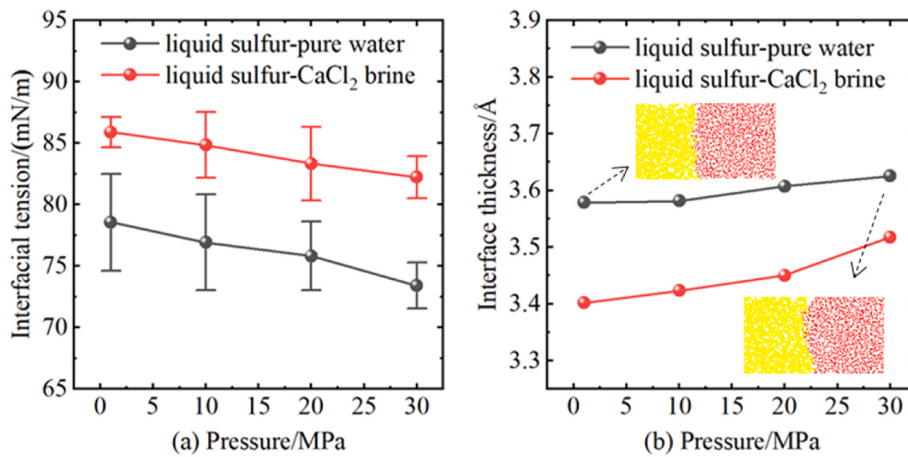


**Fig. 7.** Pressure effects on (a) interfacial tension and (b) interface thickness of liquid sulfur – formation water. The insets are the corresponding molecular snapshots at the interface.

Therefore, temperature has a more pronounced effect on interfacial tension compared to pressure.

### 3.2.3. Salinity effects

The formation water composition from Figure A1 indicates that the maximum salinity can reach 200000 mg/L. In this study, we employ CaCl<sub>2</sub> brine as a model system, maintaining the temperature and pressure at 405 K and 30 MPa, respectively. We incrementally increase the formation water salinity to determine the interfacial tension between liquid sulfur and formation water at salinities of 5000 mg/L, 100000 mg/L, and 200000 mg/L, as illustrated in Fig. 8. The data point at 0 salinity represents the interfacial tension between liquid sulfur and pure water under identical temperature and pressure conditions. The results demonstrate that interfacial tension increases significantly with rising salinity. This observation aligns with the findings from Figs. 4 and 7a. The introduction of ions enhances the force imbalance at the interface, leading to increased interfacial tension.

To understand changes in the liquid sulfur-formation water interfacial tension with salinities, we analyze the density distributions as

illustrated in Fig. 9. With temperature and pressure held constant, the sulfur density remains essentially unchanged. The interface regions on both sides of the system are demarcated by dashed lines. As salinity increases, there is a high concentration of Ca and Cl ions in the bulk water beyond the interface region, which slightly decreases the bulk water density. At a salinity of 200000 mg/L, a portion of Ca and Cl ions accumulates near the interface, with only a minimal number of ions penetrating the interface region due to the concentration gradient. Ions in the bulk water strongly interact with water molecules (as detailed in 3.2.4). Consequently, increasing salinity enhances the force imbalance at the interface, leading to a rise in interfacial tension.

### 3.2.4. Ion type effects

Based on the formation water composition shown in Figure A1, we identified additional brine types besides CaCl<sub>2</sub>, including MgCl<sub>2</sub>, Na<sub>2</sub>SO<sub>4</sub>, and NaHCO<sub>3</sub>. To comprehensively assess the impact of various salt ions on liquid sulfur-formation water interfacial tension, we employ brines with relatively high salinity. We maintain a constant temperature of 405 K and pressure of 30 MPa, ensuring consistent molar quantities of

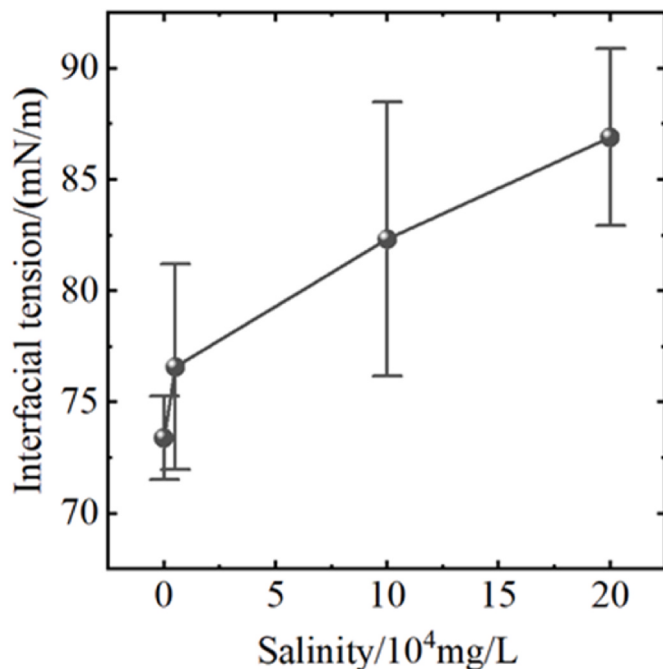


**Fig. 8.** Salinity effects on liquid sulfur – formation water interfacial tension.

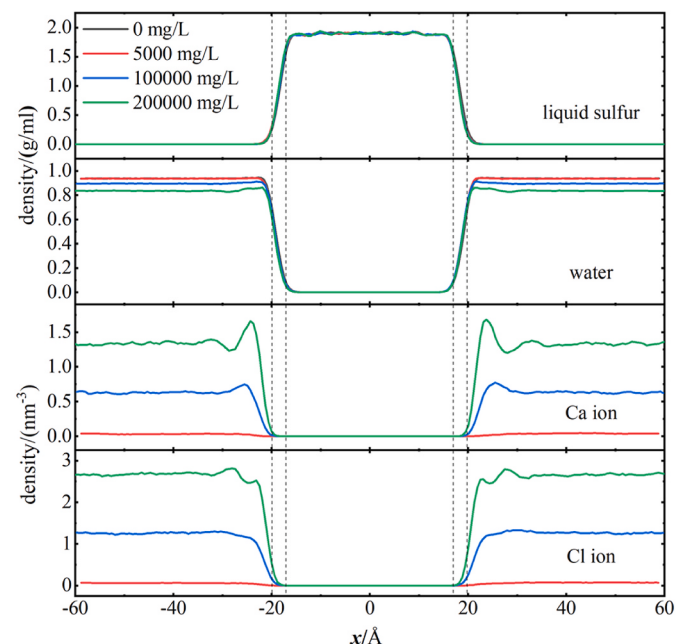


**Fig. 9.** Salinity effects on density distribution of liquid sulfur – formation water system.

water and salt across all cases.

For the  $\text{CaCl}_2$  brine at 200000 mg/L salinity, we use 174 Ca ions and 348 Cl ions. We adjust the ion amounts in the other brines accordingly: 174 Mg and 348 Cl ions in  $\text{MgCl}_2$ ; 348 Na and 174  $\text{SO}_4$  ions in  $\text{Na}_2\text{SO}_4$ ; 174 Na and 174  $\text{HCO}_3$  ions in  $\text{NaHCO}_3$ . It is important to note that due to differences in ionic masses, achieving identical salinities across all brine types is not feasible. Under conditions of equal molar quantities of water and salt, salinities range from 150000 mg/L to 250000 mg/L across the different salt solutions.

As illustrated in Fig. 10, the salt type significantly influences the liquid sulfur-formation water interfacial tension. Under identical conditions of temperature, pressure, and molarities of water and salt, the interfacial tension ranks from highest to lowest as follows:  $\text{MgCl}_2 > \text{CaCl}_2 > \text{Na}_2\text{SO}_4 > \text{NaHCO}_3$ . Moreover, the addition of any salt increases interfacial tension compared to that of liquid sulfur and pure water, which is 73.40 mN/m.

To further explore the influence of salt types on the liquid sulfur-formation water interfacial tension, we analyze the interactions between ions and water molecules using RDFs of the oxygen atom (Ow) in water molecules around different ions, as illustrated in Fig. 11.

The RDF analysis reveals that the interaction between Mg ions and water molecules is stronger than that between Ca ions and water molecules (Fig. 11a). In contrast, the interactions between Cl ions and water molecules in both  $\text{MgCl}_2$  and  $\text{CaCl}_2$  brines are comparable (Fig. 11b). This explains the higher interfacial tension observed for liquid sulfur- $\text{MgCl}_2$  brine compared to liquid sulfur- $\text{CaCl}_2$  brine.

Fig. 11b demonstrates that  $\text{SO}_4$  ions interact more strongly with water molecules than  $\text{HCO}_3$  ions. Meanwhile, Fig. 11a shows that the interactions between Na ions and water molecules are similar in both  $\text{Na}_2\text{SO}_4$  and  $\text{NaHCO}_3$  brines. Consequently, the interfacial tension between liquid sulfur and  $\text{Na}_2\text{SO}_4$  brine exceeds that between liquid sulfur and  $\text{NaHCO}_3$  brine.

Comparing Fig. 11a and b, it is evident that Ca ions interact more strongly with water molecules than Na ions, while Cl ions exhibit stronger interactions with water molecules than  $\text{SO}_4$  ions. This accounts for the higher interfacial tension observed in liquid sulfur- $\text{CaCl}_2$  brine compared to liquid sulfur- $\text{Na}_2\text{SO}_4$  brine.

These findings provide a molecular-level explanation for the observed order of interfacial tensions between liquid sulfur and various

brines, from highest to lowest:  $\text{MgCl}_2 > \text{CaCl}_2 > \text{Na}_2\text{SO}_4 > \text{NaHCO}_3$ .

For  $\text{NaHCO}_3$ , although the interaction between  $\text{HCO}_3$  ion and water molecule is slightly weaker than the interactions between water molecules themselves (Fig. 11b), the interaction between Na ions and water molecules is relatively strong (Fig. 11a). Therefore, the addition of  $\text{NaHCO}_3$  still increases the interfacial tension between liquid sulfur and water.

Our results indicate that for monatomic ions (e.g., Ca, Mg, Na, and Cl ions), ionic charge primarily governs interactions with water molecules, with higher charges yielding stronger interactions. When charges are equivalent, the ionic radius becomes the determining factor; smaller radii result in stronger interactions. For instance, the Mg ion, being smaller than the Ca ion, interacts more strongly with water. In the case of polyatomic ions (e.g.,  $\text{SO}_4$  and  $\text{HCO}_3$  ions), both charge and ionic radius play crucial roles. Although the  $\text{SO}_4$  ion has a higher charge than Cl ion, its larger ionic radius results in weaker interactions with water molecules compared to Cl ion.

### 3.3. Liquid sulfur-natural gas interfacial tension

We proceed to determine the interfacial tension between liquid sulfur and natural gas, examining the effects of temperature, pressure, and gas composition. Changes in interfacial tension are analyzed through variations in the interfacial structure.

#### 3.3.1. Temperature effects

Based on the molar composition of high-H<sub>2</sub>S natural gas (Table A1), which consists of 75 % CH<sub>4</sub>, 15 % H<sub>2</sub>S, 9 % CO<sub>2</sub>, and collectively 1 % N<sub>2</sub>, C<sub>2</sub>H<sub>6</sub> and He, we focus on the primary components. We consider CH<sub>4</sub>, H<sub>2</sub>S and CO<sub>2</sub> with adjusted molar fractions of 75 %, 15 % and 10 %, respectively. Maintaining a pressure of 30 MPa, we calculate the liquid sulfur-natural gas interfacial tensions at temperatures 395 K, 405 K, 415 K and 425 K. Fig. 12 shows that interfacial tension decreases with increasing temperature. Notably, across the temperature range, the liquid sulfur-natural gas interfacial tension consistently remains lower than both the liquid sulfur-formation water interfacial tension (Fig. 4) and the liquid sulfur surface tension (Fig. 3b).

Fig. 13a illustrates the density distribution of the liquid sulfur-natural gas system at 395 K and 30 MPa. The liquid sulfur density increases from zero in the gas phase to a plateau averaging 1.90 g/ml in the liquid sulfur phase, which is consistent with the bulk density under the same temperature and pressure conditions. The interface and its thickness between liquid sulfur and natural gas are determined using the “10–90” criterion (Xu et al., 2022), indicated by the purple dashed lines in Fig. 13a.

Progressing from the gas to the liquid sulfur phase, the CH<sub>4</sub> density initially remains constant, then rapidly increases, forming a peak near the interface before quickly decreasing to zero. H<sub>2</sub>S and CO<sub>2</sub> densities follow a similar trend, with two key differences: they form peaks within the interface region and maintain non-zero densities in the liquid sulfur phase. This behavior indicates that H<sub>2</sub>S and CO<sub>2</sub> act as “surfactants” between liquid sulfur and CH<sub>4</sub>, thereby reducing interfacial tension (as detailed in Section 3.3.3). Furthermore, the partial dissolution of H<sub>2</sub>S and CO<sub>2</sub> in liquid sulfur accounts for their non-zero densities therein.

The liquid sulfur-natural gas interface thickness at different temperatures is calculated and presented in Fig. 13b. Similar to the liquid sulfur-formation water system, the interface thickness of the liquid sulfur-natural gas system increases with rising temperature, indicating a trend toward miscibility between the two phases at higher temperatures. This increase in interface thickness reduces the force imbalance on molecules across the interface, which in turn lowers interfacial tension. A comparison of Fig. 13b with Fig. 6 reveals that the liquid sulfur-natural gas interface is thicker than the liquid sulfur-formation water interface and exhibits a more pronounced change in thickness with increasing temperature. Consequently, the interfacial tension between liquid sulfur and natural gas is lower than that between liquid sulfur and

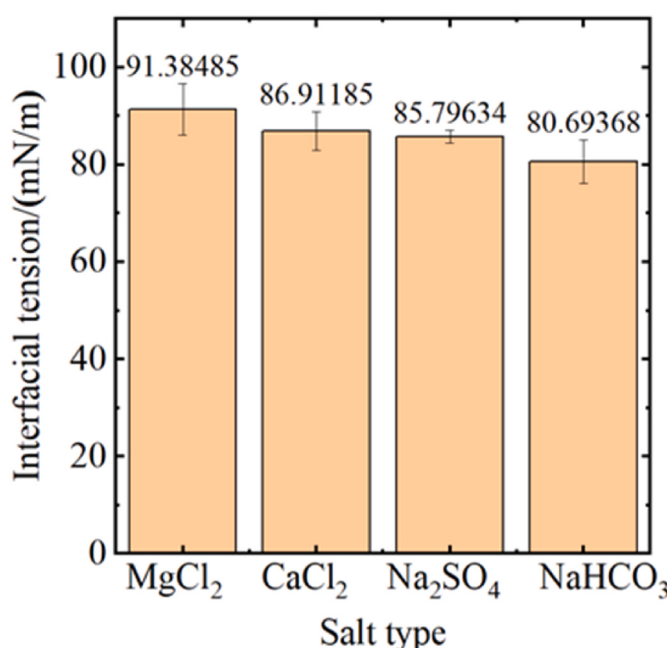
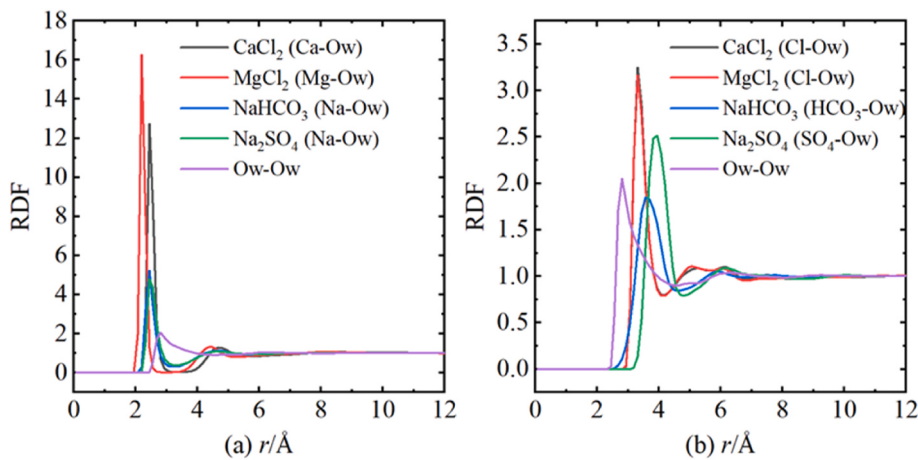
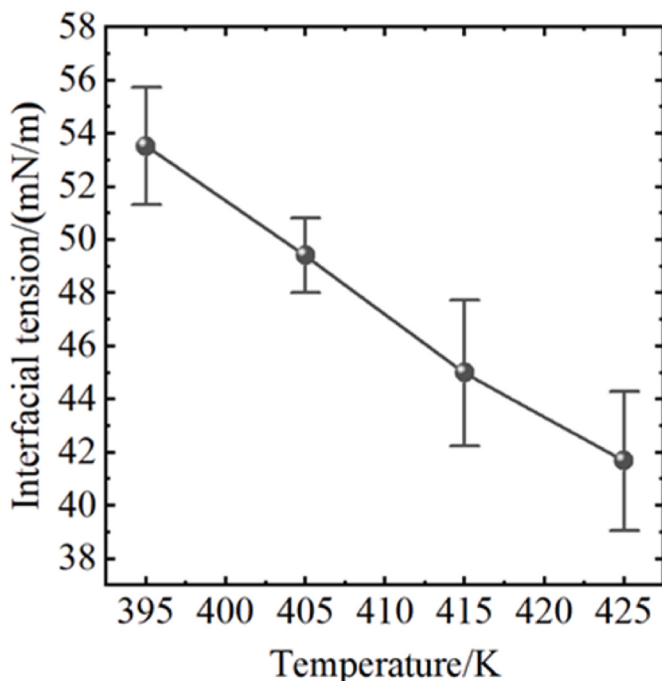


Fig. 10. Salt type effects on liquid sulfur – formation water interfacial tension.



**Fig. 11.** RDF of oxygen atom (Ow) in water molecule around different (a) cations, and (b) anions.



**Fig. 12.** Temperature effects on liquid sulfur – natural gas interfacial tension.

formation water, and it decreases more rapidly as temperature rises.

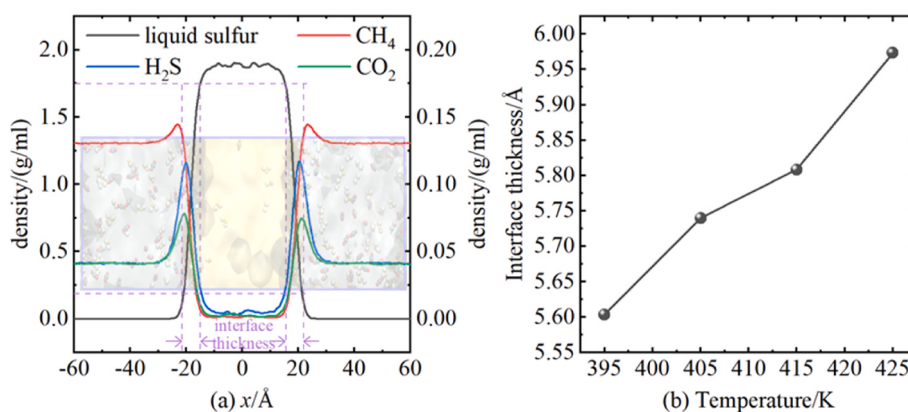
### 3.3.2. Pressure effects

Fig. 14a shows the interfacial tension between liquid sulfur and natural gas at pressures of 10 MPa, 20 MPa, and 30 MPa, while maintaining a constant temperature of 405 K. The natural gas composition is fixed at 75 % CH<sub>4</sub>, 15 % H<sub>2</sub>S, and 10 % CO<sub>2</sub>. The trends depicted in the figure indicate that the interfacial tension decreases as pressure increases from 10 MPa to 30 MPa.

Fig. 14b illustrates the interface thickness between liquid sulfur and natural gas as a function of pressure. An increase in pressure corresponds to an increase in interface thickness. This suggests enhanced miscibility between liquid sulfur and natural gas, which leads to reduced interfacial tension. Comparative analysis of Figs. 14b and 13b reveals that, unlike the liquid sulfur-formation water system, pressure exerts a comparable influence to temperature on the interface thickness of the liquid sulfur-natural gas system. This phenomenon can be attributed to the higher compressibility of natural gas in comparison to formation water.

### 3.3.3. Gas composition effects

Given that the primary components of high-H<sub>2</sub>S natural gas are CH<sub>4</sub>, H<sub>2</sub>S and CO<sub>2</sub>, it is essential to investigate the interfacial tension between liquid sulfur and natural gas with varying gas compositions. We calculate the liquid sulfur-CH<sub>4</sub> interfacial tension at 405 K and 30 MPa, ensuring that the molar quantity of CH<sub>4</sub> aligns with the CH<sub>4</sub>/H<sub>2</sub>S/CO<sub>2</sub> mixture detailed in Sections 3.3.1 and 3.3.2. Subsequently, we determine the interfacial tensions of the liquid sulfur-CH<sub>4</sub>/CO<sub>2</sub> and liquid sulfur-CH<sub>4</sub>/H<sub>2</sub>S by introducing different molar amounts of CO<sub>2</sub> and H<sub>2</sub>S into the liquid sulfur-CH<sub>4</sub> systems. Additionally, we add various molar



**Fig. 13.** (a) Density distribution and (b) temperature effects on interface thickness of liquid sulfur – natural gas systems.

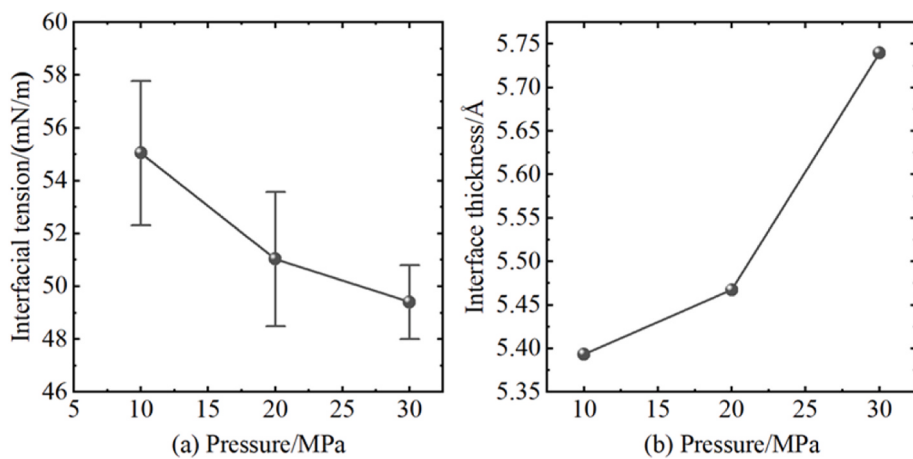


Fig. 14. Pressure effects on (a) interfacial tension and (b) interface thickness of liquid sulfur – natural gas systems.

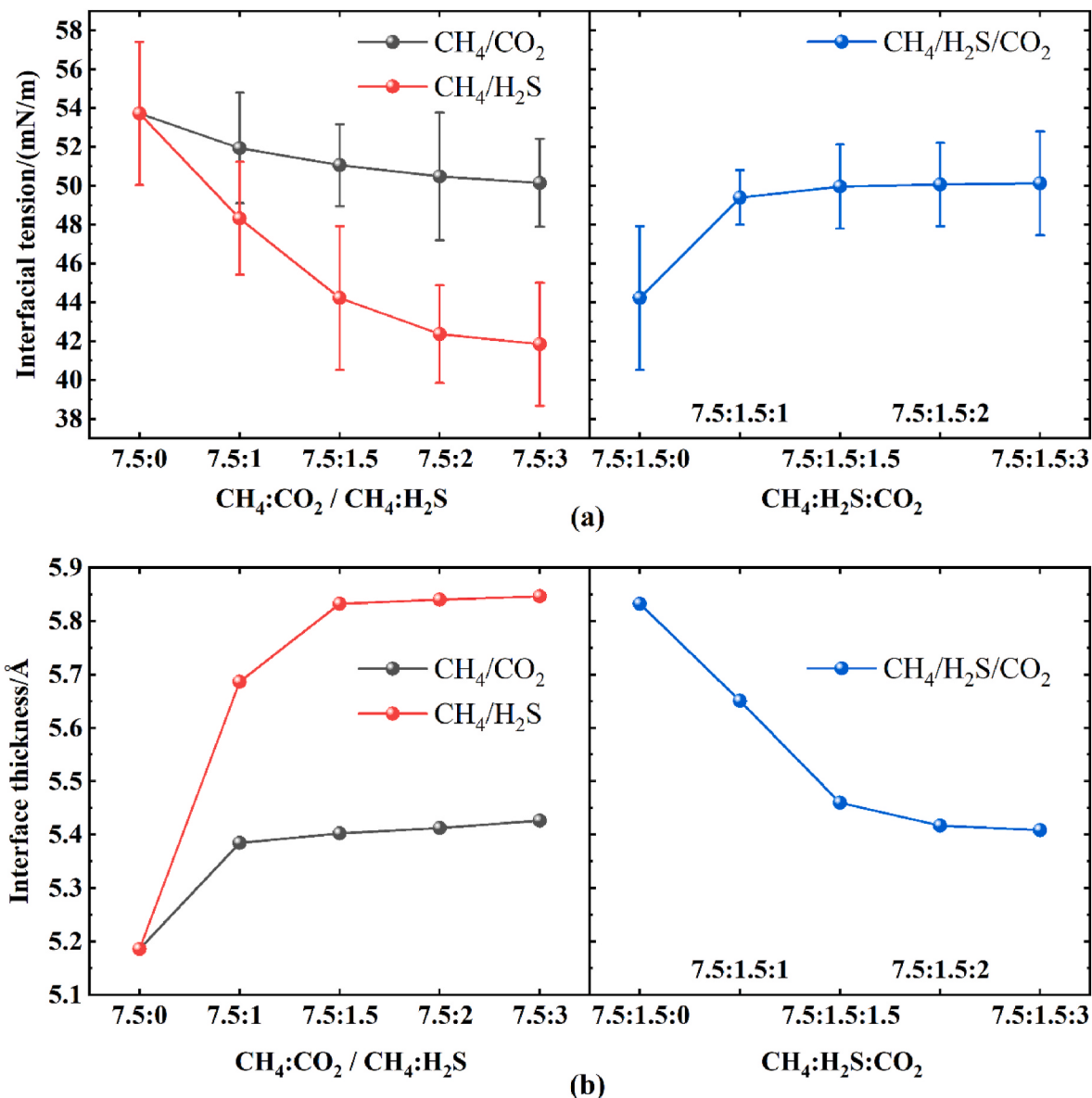


Fig. 15. Gas composition effects on (a) interfacial tension and (b) interface thickness of liquid sulfur – natural gas systems.

amounts of CO<sub>2</sub> into the liquid sulfur-H<sub>2</sub>S system to calculate interfacial tensions for different H<sub>2</sub>S:CO<sub>2</sub> ratios. The results are presented in Fig. 15a.

The liquid sulfur-CH<sub>4</sub> system exhibits the highest interfacial tension among the studied compositions. The addition of CO<sub>2</sub> and H<sub>2</sub>S effectively reduces the interfacial tension between liquid sulfur and natural gas, which explains their distribution within the interface region of the liquid sulfur-natural gas system, as depicted in Fig. 13a. The interfacial tensions decrease with increased CO<sub>2</sub> and H<sub>2</sub>S ratios, though the rate of decrease slows over time. Notably, H<sub>2</sub>S demonstrates a more pronounced effect on reducing interfacial tension compared to an equivalent amount of CO<sub>2</sub>. This is primarily due to the higher solubility of liquid sulfur in H<sub>2</sub>S (Li et al., 2018). Conversely, introducing additional CO<sub>2</sub> into the CH<sub>4</sub>/H<sub>2</sub>S system results in an increase in interfacial tension. As the CO<sub>2</sub> ratio increases, the interfacial tension increases and approaches the characteristic value of the liquid sulfur-CH<sub>4</sub>/CO<sub>2</sub> system.

Fig. 15b illustrates the calculated interface thickness between liquid sulfur and natural gas with varying compositions. The liquid sulfur-CH<sub>4</sub> system exhibits the smallest interface thickness. The addition of CO<sub>2</sub> and H<sub>2</sub>S increases the interface thickness, indicating enhanced miscibility between liquid sulfur and natural gas, which in turn reduces interfacial tension. The liquid sulfur-CH<sub>4</sub>/H<sub>2</sub>S system demonstrates the greatest interface thickness, consistent with the higher solubility of liquid sulfur in H<sub>2</sub>S. Notably, when CO<sub>2</sub> is introduced to the CH<sub>4</sub>/H<sub>2</sub>S system, the interface thickness decreases. This observation suggests that CO<sub>2</sub>

addition reduces the solubility of liquid sulfur in the CH<sub>4</sub>/H<sub>2</sub>S mixture, thereby increasing interfacial tension.

To further elucidate the effect of natural gas compositions on interfacial tension, we calculate the density distributions of liquid sulfur-natural gas systems with various compositions, as illustrated in Fig. 16. Additionally, Figure A11 provides molecular snapshots of the four systems for visual reference. The liquid sulfur-CH<sub>4</sub> system exhibits a density peak near the interface, indicating CH<sub>4</sub> adsorption, with 33.44 % of CH<sub>4</sub> molecules located in the interface region. Upon the addition of CO<sub>2</sub> or H<sub>2</sub>S, these components preferentially adsorb near the interface, reducing the CH<sub>4</sub> density peak. The proportion of CH<sub>4</sub> in the interface region decreases to 31.83 % with CO<sub>2</sub> and 29.69 % with H<sub>2</sub>S. By comparison, 42.80 % of CO<sub>2</sub> and 49.03 % of H<sub>2</sub>S are adsorbed at the interface.

The introduction of CO<sub>2</sub> into the liquid sulfur-CH<sub>4</sub>/H<sub>2</sub>S system leads to competitive adsorption between CO<sub>2</sub> and H<sub>2</sub>S, partially suppressing the density peak of H<sub>2</sub>S. This reduces the H<sub>2</sub>S adsorption from 49.03 % to 46.01 %. Since H<sub>2</sub>S exhibits the strongest effect on reducing interfacial tension, the addition of CO<sub>2</sub> to the CH<sub>4</sub>/H<sub>2</sub>S system paradoxically increases the interfacial tension.

#### 4. Conclusions

This study represents a comprehensive investigation of the IFT between liquid sulfur and formation water/natural gas under in-situ

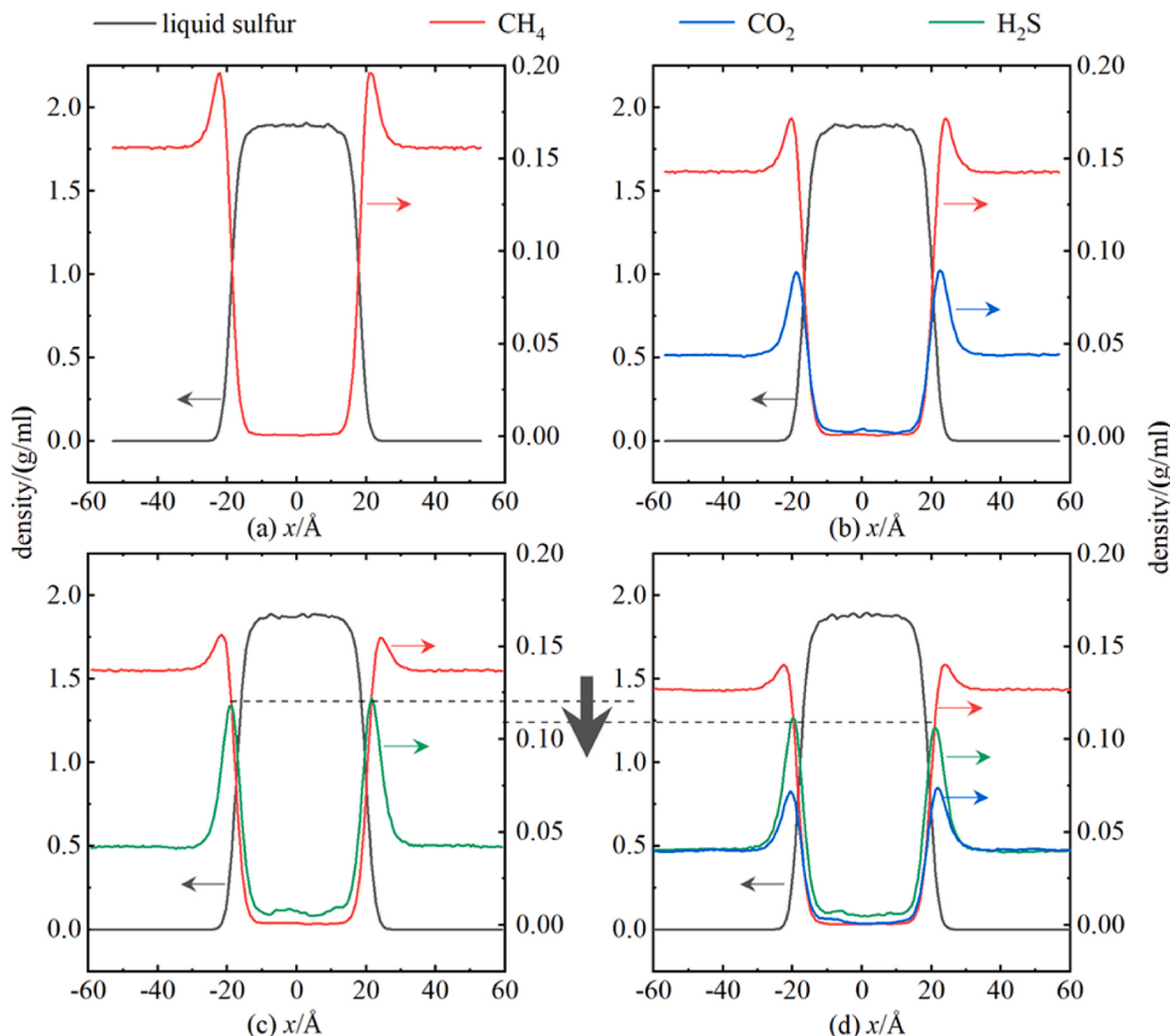


**Fig. 16.** Density distribution of (a) liquid sulfur – CH<sub>4</sub>, (b) liquid sulfur – CH<sub>4</sub>/CO<sub>2</sub> (CH<sub>4</sub>:CO<sub>2</sub> = 7.5:1), (c) liquid sulfur – CH<sub>4</sub>/H<sub>2</sub>S (CH<sub>4</sub>:H<sub>2</sub>S = 7.5:1.5), and (d) liquid sulfur – CH<sub>4</sub>/H<sub>2</sub>S/CO<sub>2</sub> (CH<sub>4</sub>:H<sub>2</sub>S:CO<sub>2</sub> = 7.5:1.5:1) systems.

conditions, a critical yet previously understudied area. Using validated molecular models and MD simulations, we analyzed surface and interfacial tensions while systematically exploring the effects of temperature, pressure, salinity, ion type, and gas composition. The main conclusions are as follows.

- (1) The constructed models for liquid sulfur, natural gas, and formation water demonstrate agreement with reference data for density, viscosity, and surface tension. This confirms the reliability of the force field and simulation methodology.
- (2) Within the simulated temperature range (395–425 K), liquid sulfur-formation water interfacial tension exceeds liquid sulfur surface tension, which in turn surpassed liquid sulfur-natural gas interfacial tension. This primarily results from force imbalances at the interfaces. As temperatures increases, both surface tensions and interfacial tensions decrease due to enhanced molecular kinetic energy, reduced bulk phase cohesion, improved miscibility, and diminished interfacial force imbalances.
- (3) Increasing pressure (1–30 MPa) reduces the interfacial tensions of both liquid sulfur-formation water and liquid sulfur-natural gas systems, a result of enhanced miscibility and diminished interfacial force imbalances. The effect is more pronounced in the liquid sulfur-natural gas system, likely due to the higher compressibility of natural gas.
- (4) The presence of ions significantly increases liquid sulfur-formation water interfacial tension, with greater increases observed at higher salinities (5000–200000 mg/L). This effect stems from the distribution of ions in the bulk water and their strong interactions with water molecules, which enhance the interfacial force imbalance.
- (5) Different ions contribute to varying increases in interfacial tension. Under specific conditions of temperature, pressure, and salinity, the liquid sulfur-brine interfacial tensions rank as follows:  $MgCl_2 > CaCl_2 > Na_2SO_4 > NaHCO_3$ . This order reflects the strength of ion-water interactions, influenced by ionic charge and radius.
- (6) Natural gas composition affects the liquid sulfur-natural gas interfacial tension, with the highest values observed for pure  $CH_4$ . The addition of  $H_2S$  or  $CO_2$  to  $CH_4$  reduces interfacial tension, with  $H_2S$  exerting the strongest effect. This reduction occurs because  $CO_2$  and  $H_2S$  primarily localize at the interface, weakening the force imbalance. However, in the liquid sulfur- $CH_4/H_2S$  system, interfacial tension is higher than in the liquid sulfur- $CH_4/H_2S$  system due to competitive adsorption between  $CO_2$  and  $H_2S$  at the interface, which diminishes  $H_2S$ 's ability to reduce interfacial tension.

## Appendix A. Supplementary material

**Table A1**  
Composition of natural gas

| Component        | $CH_4$ | $H_2S$ | $CO_2$ | $(N_2+C_2H_6+He)$ |
|------------------|--------|--------|--------|-------------------|
| Molar fraction/% | 75     | 15     | 9      | 1                 |

This study establishes a foundational framework with reliable molecular models for future molecular simulations of high- $H_2S$  natural gas reservoirs. By addressing the lack of IFT data for liquid sulfur-formation water/natural gas under in-situ conditions, it delivers critical IFT inputs for meso- and macroscale numerical simulations. As IFT governs fluid flow and saturation distribution, it becomes possible to more accurately simulate sulfur deposition patterns and accumulation zones under varying geological and engineering conditions. This is essential for identifying regions at risk of flow blockages or production impairment due to sulfur deposition. Simulation results provide practical guidance for operators, such as optimizing well placement, refining drilling trajectories, and adjusting production pressure, to either mitigate deposition or leverage it to maintain efficient production. As such, this study not only advances the understanding of interfacial phenomena but also provides practical insights to enhance the development of high- $H_2S$  reservoirs.

## CRediT authorship contribution statement

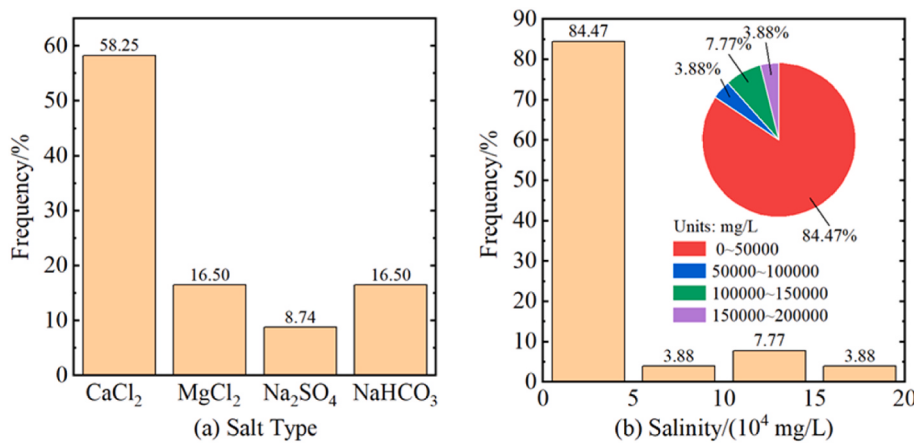
**Zheng Li:** Writing – original draft, Visualization, Validation, Software, Methodology, Data curation, Conceptualization. **Daqian Zeng:** Resources, Funding acquisition, Conceptualization. **Tong Li:** Supervision, Investigation, Data curation. **Qian Li:** Writing – review & editing, Validation, Data curation. **Rui Zhang:** Resources, Project administration. **Liang Huang:** Validation, Software. **Xiaoguang Wang:** Writing – review & editing, Visualization. **Heng Wang:** Writing – review & editing, Formal analysis.

## Declaration of competing interest

The authors declare that they have no known competing financial interests or personal relationships that could have appeared to influence the work reported in this paper.

## Acknowledgements

This work is supported by the National Natural Science Foundation of China (grant number 52204032), the Natural Science Foundation of Sichuan Province (grant number 2024NSFSC0978), the open fund project of “Molecular Simulation of Gas-Water-Sulfur Multiphase Interface Characteristics and Microscopic Flow Mechanisms in High-Sulfur Gas Reservoirs” from the SINOPEC Key Laboratory of Marine Oil & Gas Reservoirs Production (grant number 33550000-22-ZC0613-0273), and the Science & Technology Department of Sichuan Province (grant number 2022YFSY0008).

**Fig. A1.** Composition of formation water: (a) salt types and (b) salt concentrations.**Table A2**  
Force field parameters for CH<sub>4</sub>

| Non-bonded parameters |                    |                                  |                            |          |
|-----------------------|--------------------|----------------------------------|----------------------------|----------|
| Atom                  | Molar mass/(g/mol) | $\sigma/\text{\AA}$              | $\epsilon/\text{kcal/mol}$ | Charge/e |
| C                     | 12.011             | 3.5                              | 0.066                      | -0.24    |
| H                     | 1.008              | 2.5                              | 0.03                       | 0.06     |
| Bond parameters       |                    |                                  |                            |          |
| Bond                  |                    | $K_b/(\text{kcal}/\text{\AA}^2)$ | $r_0/\text{\AA}$           |          |
| C—H                   |                    | 340                              | 1.09                       |          |
| Angle parameters      |                    |                                  |                            |          |
| Angle                 |                    | $K_a/(\text{kcal}/\text{rad}^2)$ | $\theta/^\circ$            |          |
| H—C—H                 |                    | 33                               | 107.8                      |          |

**Table A3**  
Force field parameters for H<sub>2</sub>S

| Non-bonded parameters |                    |                                  |                            |          |
|-----------------------|--------------------|----------------------------------|----------------------------|----------|
| Atom                  | Molar mass/(g/mol) | $\sigma/\text{\AA}$              | $\epsilon/\text{kcal/mol}$ | Charge/e |
| H                     | 1.008              | 0.98                             | 0.00775                    | 0.124    |
| S                     | 32.06              | 3.72                             | 0.497                      | -0.248   |
| SH                    | -                  | 2.15                             | 0.06206                    | -        |
| Bond parameters       |                    |                                  |                            |          |
| Bond                  |                    | $K_b/(\text{kcal}/\text{\AA}^2)$ | $r_0/\text{\AA}$           |          |
| S—H                   |                    | 95.805                           | 1.365                      |          |
| Angle parameters      |                    |                                  |                            |          |
| Angle                 |                    | $K_a/(\text{kcal}/\text{rad}^2)$ | $\theta/^\circ$            |          |
| H—S—H                 |                    | 62.05                            | 91.5                       |          |

**Table A4**  
Force field parameters for CO<sub>2</sub>

| Non-bonded parameters |                    |                                  |                            |          |
|-----------------------|--------------------|----------------------------------|----------------------------|----------|
| Atom                  | Molar mass/(g/mol) | $\sigma/\text{\AA}$              | $\epsilon/\text{kcal/mol}$ | Charge/e |
| C                     | 12.011             | 2.8                              | 0.0536                     | 0.7      |
| O                     | 15.9994            | 3.05                             | 0.1569                     | -0.35    |
| Bond parameters       |                    |                                  |                            |          |
| Bond                  |                    | $K_b/(\text{kcal}/\text{\AA}^2)$ | $r_0/\text{\AA}$           |          |
| C—O                   |                    | 0                                | 1.16                       |          |
| Angle parameters      |                    |                                  |                            |          |
| Angle                 |                    | $K_a/(\text{kcal}/\text{rad}^2)$ | $\theta/^\circ$            |          |
| O—C—O                 |                    | 0                                | 180                        |          |

**Table A5**  
Force field parameters for H<sub>2</sub>O

| Non-bonded parameters |                    |                                  |                            |          |
|-----------------------|--------------------|----------------------------------|----------------------------|----------|
| Atom                  | Molar mass/(g/mol) | $\sigma/\text{\AA}$              | $\epsilon/\text{kcal/mol}$ | Charge/e |
| H                     | 1.008              | 0.0                              | 0.0                        | 0.4238   |
| O                     | 15.9994            | 3.166                            | 0.1553                     | -0.8476  |
| Bond parameters       |                    |                                  |                            |          |
| Bond                  |                    | $K_b/(\text{kcal}/\text{\AA}^2)$ | $r_0/\text{\AA}$           |          |
| O—H                   |                    | 553.858                          | 1.0                        |          |
| Angle parameters      |                    |                                  |                            |          |
| Angle                 |                    | $K_a/(\text{kcal}/\text{rad}^2)$ | $\theta/^\circ$            |          |
| H—O—H                 |                    | 45.735                           | 109.47                     |          |

**Table A6**  
Force field parameters for ions

| Non-bonded parameters                |                    |                     |                            |          |
|--------------------------------------|--------------------|---------------------|----------------------------|----------|
| Atom                                 | Molar mass/(g/mol) | $\sigma/\text{\AA}$ | $\epsilon/\text{kcal/mol}$ | Charge/e |
| Ca                                   | 40.08              | 2.872               | 0.1                        | 2.0      |
| Mg                                   | 24.305             | 1.64448             | 0.874983                   | 2.0      |
| Na(NaHCO <sub>3</sub> )              | 22.98977           | 2.351               | 0.1301                     | 1.0      |
| Na(Na <sub>2</sub> SO <sub>4</sub> ) | 22.98977           | 2.58                | 0.1                        | 1.0      |
| Cl                                   | 35.453             | 4.4018              | 0.1001                     | -1.0     |
| O1(HCO <sub>3</sub> )                | 15.9994            | 3.1656              | 0.15528566                 | -0.7907  |
| O2(HCO <sub>3</sub> )                | 15.9994            | 3.1656              | 0.15528566                 | -0.8985  |
| O3(HCO <sub>3</sub> )                | 15.9994            | 3.1656              | 0.15528566                 | -0.8338  |
| C(HCO <sub>3</sub> )                 | 12.011             | 2.4044              | 0.021358497                | 1.123    |
| H(HCO <sub>3</sub> )                 | 1.008              | 2.058               | 0.0                        | 0.4000   |
| O(SO <sub>4</sub> )                  | 15.9994            | 3.916               | 0.0239                     | -1.0     |
| S(SO <sub>4</sub> )                  | 32.06              | 3.55                | 0.25012                    | 2.0      |

**Table A7**  
Force field parameters for S<sub>8</sub>

| Non-bonded parameters |                    |                                  |                            |          |
|-----------------------|--------------------|----------------------------------|----------------------------|----------|
| Atom                  | Molar mass/(g/mol) | $\sigma/\text{\AA}$              | $\epsilon/\text{kcal/mol}$ | Charge/e |
| S                     | 32.06              | 3.36                             | 0.44                       | 0.0      |
| Bond parameters       |                    |                                  |                            |          |
| Bond                  |                    | $K_b/(\text{kcal}/\text{\AA}^2)$ | $r_0/\text{\AA}$           |          |
| S—S                   |                    | 105                              | 2.109                      |          |
| Angle parameters      |                    |                                  |                            |          |
| Angle                 |                    | $K_a/(\text{kcal}/\text{rad}^2)$ | $\theta/^\circ$            |          |
| S—S—S                 |                    | 60                               | 109.492                    |          |
| Dihedral parameters   |                    |                                  |                            |          |
| Dihedral              | A1                 | A2                               | A3                         | A4       |
| S—S—S—S               | -23.5204           | 7.2152                           | 95.1980                    | -5.8431  |
|                       |                    |                                  |                            | -64.2096 |

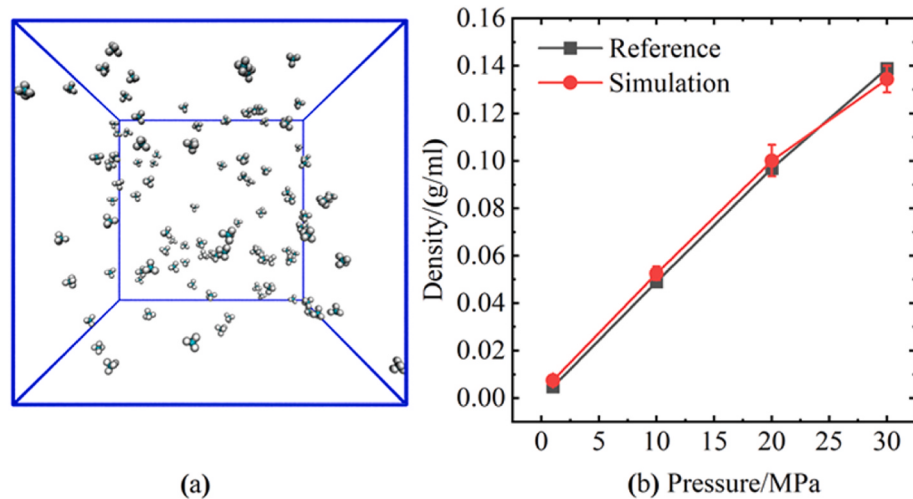


**Fig. A2.** (a) MD simulation system for density calculation and (b) comparison of simulation results with reference data ([National Institute of Standards and Technology, 2024](#)) for CH<sub>4</sub>.

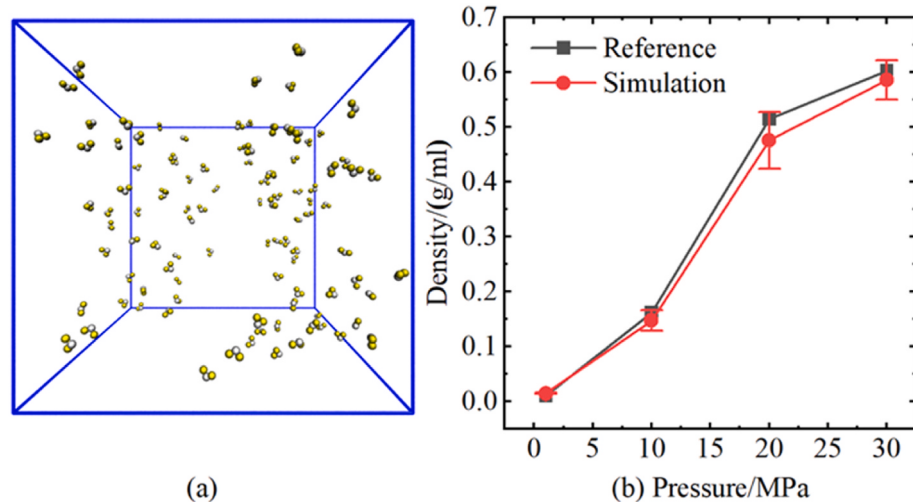


**Fig. A3.** (a) MD simulation system for density calculation and (b) comparison of simulation results with reference data ([National Institute of Standards and Technology, 2024](#)) for H<sub>2</sub>S.

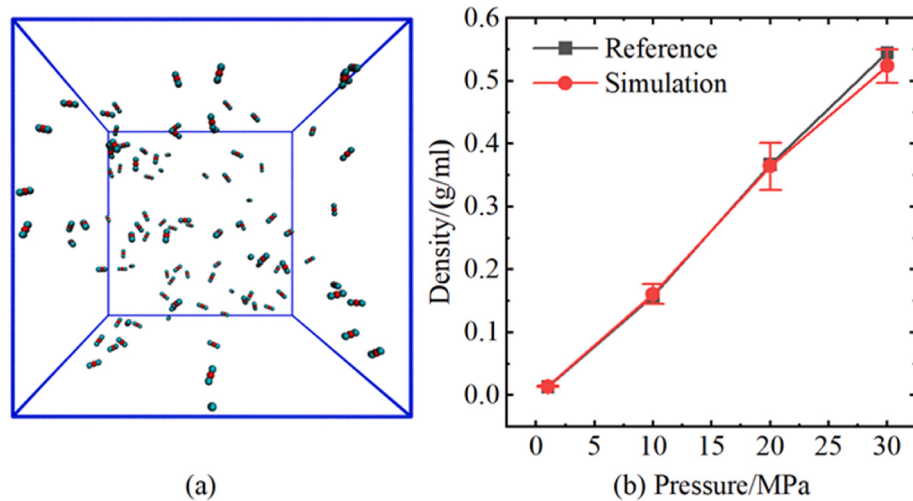


**Fig. A4.** (a) MD simulation system for density calculation and (b) comparison of simulation results with reference data ([National Institute of Standards and Technology, 2024](#)) for CO<sub>2</sub>.

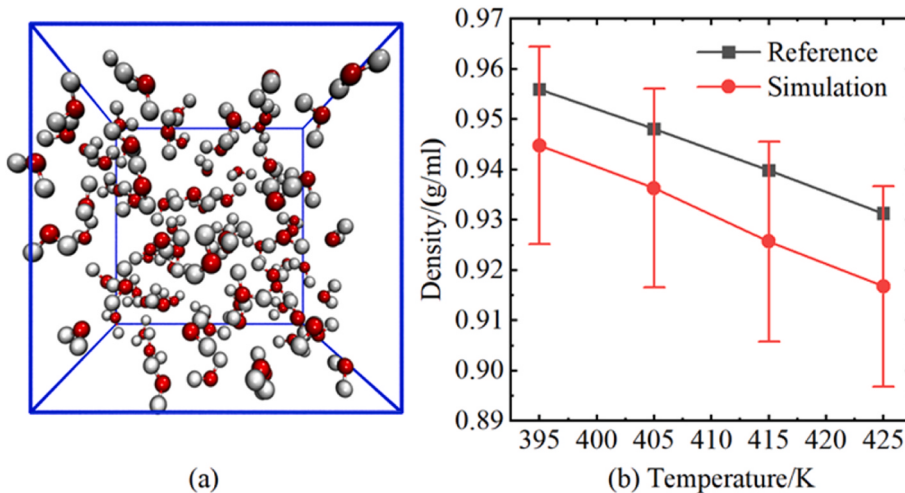


**Fig. A5.** (a) MD simulation system for density calculation and (b) comparison of simulation results with reference data ([National Institute of Standards and Technology, 2024](#)) for H<sub>2</sub>O.

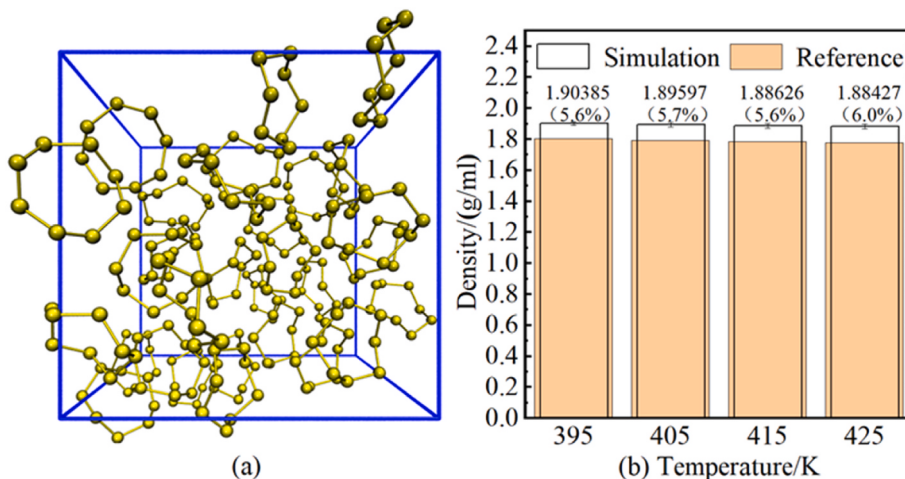


**Fig. A6.** (a) MD simulation system for density calculation and (b) comparison of simulation results with reference data ([Espeau and Céolin, 2007](#); [Fanelli, 1950](#)) for S<sub>8</sub>.

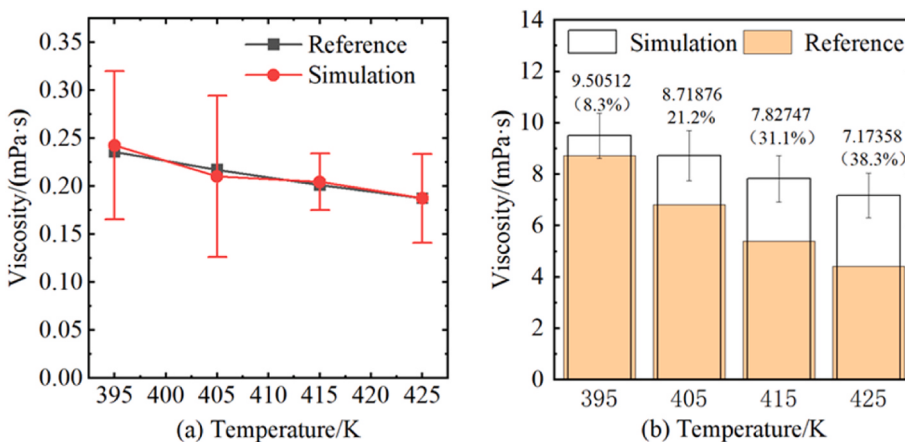


**Fig. A7.** Comparison of simulation results with reference data ([Bacon and Fanelli, 1943](#); [National Institute of Standards and Technology, 2024](#)) for (a) water viscosity and (b) S<sub>8</sub> viscosity.

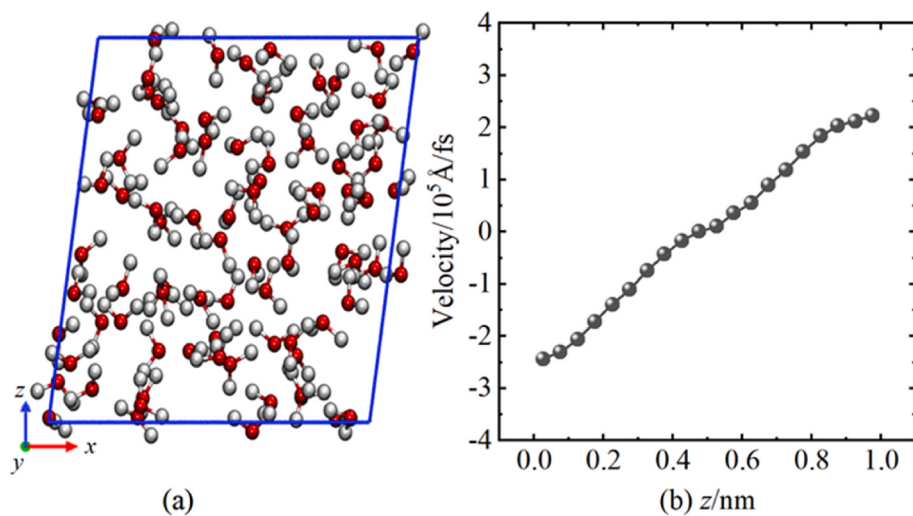


**Fig. A8.** (a) MD simulation system and (b) equilibrium velocity distribution for water viscosity calculation.

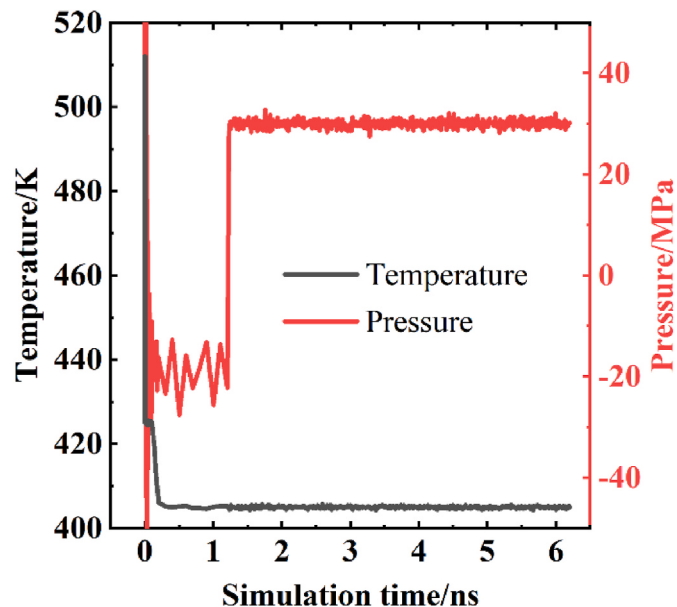


**Fig. A9.** Variation of temperature and pressure with simulation time.

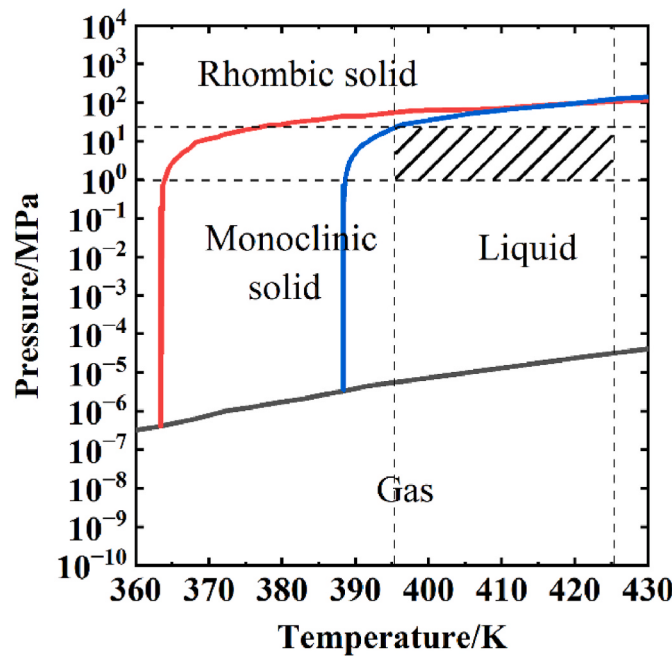


**Fig. A10.** Phase diagram of sulfur. The shaded area indicates the temperature and pressure conditions investigated in this study.

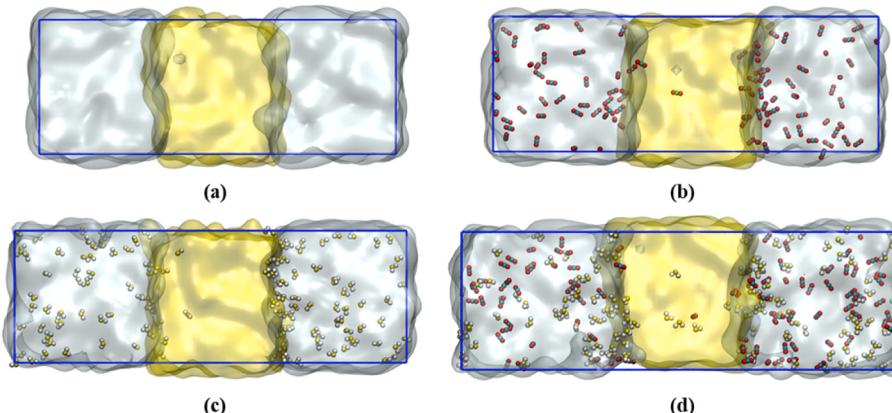


**Fig. A11.** Molecular snapshots of (a) liquid sulfur –  $\text{CH}_4$ , (b) liquid sulfur –  $\text{CH}_4/\text{CO}_2$  ( $\text{CH}_4:\text{CO}_2 = 7.5:1$ ), (c) liquid sulfur –  $\text{CH}_4/\text{H}_2\text{S}$  ( $\text{CH}_4:\text{H}_2\text{S} = 7.5:1.5$ ), and (d) liquid sulfur –  $\text{CH}_4/\text{H}_2\text{S}/\text{CO}_2$  ( $\text{CH}_4:\text{H}_2\text{S}:\text{CO}_2 = 7.5:1.5:1$ ) systems.  $\text{S}_8$  and  $\text{CH}_4$  molecules are rendered with transparency for clarity.

**Table A8**  
Summary for liquid sulfur-formation water interfacial tensions

| T/K | P/MPa | Brine                    | Salinity/(mg/L) | IFTs/(mN/m)      |
|-----|-------|--------------------------|-----------------|------------------|
| 395 | 30    | –                        | –               | $76.47 \pm 3.89$ |
| 405 | 30    | –                        | –               | $73.40 \pm 1.88$ |
| 415 | 30    | –                        | –               | $70.82 \pm 3.32$ |
| 425 | 30    | –                        | –               | $67.65 \pm 1.95$ |
| 405 | 1     | –                        | –               | $78.55 \pm 3.94$ |
| 405 | 10    | –                        | –               | $76.90 \pm 3.90$ |
| 405 | 20    | –                        | –               | $75.81 \pm 2.79$ |
| 395 | 30    | $\text{CaCl}_2$          | 50000           | $84.23 \pm 3.84$ |
| 405 | 30    | $\text{CaCl}_2$          | 50000           | $82.22 \pm 1.72$ |
| 415 | 30    | $\text{CaCl}_2$          | 50000           | $77.99 \pm 3.19$ |
| 425 | 30    | $\text{CaCl}_2$          | 50000           | $75.66 \pm 3.15$ |
| 405 | 1     | $\text{CaCl}_2$          | 50000           | $85.91 \pm 1.24$ |
| 405 | 10    | $\text{CaCl}_2$          | 50000           | $84.85 \pm 2.68$ |
| 405 | 20    | $\text{CaCl}_2$          | 50000           | $83.33 \pm 2.99$ |
| 405 | 30    | $\text{CaCl}_2$          | 5000            | $76.58 \pm 4.61$ |
| 405 | 30    | $\text{CaCl}_2$          | 100000          | $82.33 \pm 6.16$ |
| 405 | 30    | $\text{CaCl}_2$          | 200000          | $86.91 \pm 3.99$ |
| 405 | 30    | $\text{MgCl}_2$          | 170000          | $91.38 \pm 5.23$ |
| 405 | 30    | $\text{Na}_2\text{SO}_4$ | 250000          | $85.80 \pm 1.35$ |
| 405 | 30    | $\text{NaHCO}_3$         | 150000          | $80.69 \pm 4.47$ |

**Table A9**  
Summary for liquid sulfur-natural gas interfacial tensions

| T/K | P/MPa | Composition (CH <sub>4</sub> :H <sub>2</sub> S:CO <sub>2</sub> ) | IFTs/(mN/m)  |
|-----|-------|--|--------------|
| 395 | 30    | 7.5:1.5:1.0  | 53.52 ± 2.21 |
| 405 | 30    | 7.5:1.5:1.0  | 49.40 ± 1.40 |
| 415 | 30    | 7.5:1.5:1.0  | 44.99 ± 2.75 |
| 425 | 30    | 7.5:1.5:1.0  | 41.68 ± 2.62 |
| 405 | 10    | 7.5:1.5:1.0  | 55.04 ± 2.73 |
| 405 | 20    | 7.5:1.5:1.0  | 51.03 ± 2.55 |
| 405 | 30    | 7.5:0.0:0.0  | 53.72 ± 3.68 |
| 405 | 30    | 7.5:0.0:1.0  | 51.95 ± 2.85 |
| 405 | 30    | 7.5:0.0:1.5  | 51.06 ± 2.11 |
| 405 | 30    | 7.5:0.0:2.0  | 50.48 ± 3.28 |
| 405 | 30    | 7.5:0.0:3.0  | 50.15 ± 2.26 |
| 405 | 30    | 7.5:1:0:0.0  | 48.33 ± 2.91 |
| 405 | 30    | 7.5:1:5:0.0  | 44.23 ± 3.69 |
| 405 | 30    | 7.5:2:0:0.0  | 42.37 ± 2.52 |
| 405 | 30    | 7.5:3:0:0.0  | 41.84 ± 3.17 |
| 405 | 30    | 7.5:1:5:1.5  | 49.96 ± 2.17 |
| 405 | 30    | 7.5:1:5:2.0  | 50.08 ± 2.15 |
| 405 | 30    | 7.5:1:5:3.0  | 50.13 ± 2.67 |

## Data availability

Data will be made available on request.

## References

- Aggelopoulos, C.A., Robin, M., Perfetti, E., Vizika, O., 2010. CO<sub>2</sub>/CaCl<sub>2</sub> solution interfacial tensions under CO<sub>2</sub> geological storage conditions: influence of cation valence on interfacial tension. *Adv. Water Resour.* 33, 691–697. <https://doi.org/10.1016/j.advwatres.2010.04.006>.
- Alejandre, J., Tildesley, D.J., Chapel, G.A., 1995. Molecular dynamics simulation of the orthobaric densities and surface tension of water. *J. Chem. Phys.* 102, 4574–4583. <https://doi.org/10.1063/1.469505>.
- Bachu, S., Bennion, D.B., 2009. Interfacial tension between CO<sub>2</sub>, freshwater, and brine in the range of pressure from (2 to 27) MPa, temperature from (20 to 125) °C, and water salinity from (0 to 334 000) mg·L<sup>-1</sup>. *J. Chem. Eng. Data* 54, 765–775. <https://doi.org/10.1021/je800529x>.
- Bacon, R.F., Fanelli, R., 1943. The viscosity of sulfur. *J. Am. Chem. Soc.* 65, 639–648. <https://doi.org/10.1021/ja01244a043>.
- Ballone, P., Jones, R., 2003. Density functional and Monte Carlo studies of sulfur. II. Equilibrium polymerization of the liquid phase. *J. Chem. Phys.* 119, 8704–8715. <https://doi.org/10.1063/1.1611475>.
- Berendsen, H., Grigera, J., Straatsma, T., 1987. The missing term in effective pair potentials. *J. Phys. Chem.* 91, 6269–6271. <https://doi.org/10.1021/j100308a038>.
- Berry, J.D., Neeson, M.J., Dagastine, R.R., Chan, D.Y., Tabor, R.F., 2015. Measurement of surface and interfacial tension using pendant drop tensiometry. *J. Colloid Interface Sci.* 454, 226–237. <https://doi.org/10.1016/j.jcis.2015.05.012>.
- Cai, J., Qin, X., Wang, H., Xia, Y., Zou, S., 2025. Pore-scale investigation of forced imbibition in porous rocks through interface curvature and pore topology analysis. *J. Rock Mech. Geotech. Eng.* 17, 245–257. <https://doi.org/10.1016/j.jrmge.2024.02.047>.
- Cai, J., Jin, T., Kou, J., Zou, S., Xiao, J., Meng, Q., 2021. Lucas–Washburn equation-based modeling of capillary-driven flow in porous systems. *Langmuir* 37, 1623–1636. <https://doi.org/10.1021/acs.langmuir.0c03134>.
- Caو, Y., Lu, L., Chen, W., 2024. Dynamic gas liberation from water-immersed anthracite coal with varying wetting states under heating conditions: unveiling the gas breakthrough phenomena. *Gas Sci. Eng.* 122, 205205. <https://doi.org/10.1016/j.jgsce.2024.205205>.
- Castro, P.S., Zuniga, G.M., Holmes, W., Buchireddy, P.R., Gang, D.D., Revellame, E., Zappi, M., Hernandez, R., 2023. Review of the adsorbents/catalysts for the removal of sulfur compounds from natural gas. *Gas Sci. Eng.* 115, 205004. <https://doi.org/10.1016/j.jgsce.2023.205004>.
- Chen, C., Chai, Z., Shen, W., Li, W., Song, Y., 2017. Wettability of supercritical CO<sub>2</sub>-brine-mineral: the effects of ion type and salinity. *Energy Fuels* 31, 7317–7324. <https://doi.org/10.1021/acs.energyfuels.7b00840>.
- Chi, Y., Xu, Y., Zhao, C., Zhang, Y., Song, Y., 2022. In-situ measurement of interfacial tension: further insights into effect of interfacial tension on the kinetics of CO<sub>2</sub> hydrate formation. *Energy* 239, 122143. <https://doi.org/10.1016/j.energy.2021.122143>.
- Chiquet, P., Daridon, J.L., Broseta, D., Thibeau, S., 2007. CO<sub>2</sub>/water interfacial tensions under pressure and temperature conditions of CO<sub>2</sub> geological storage. *Energy Convers. Manag.* 48, 736–744. <https://doi.org/10.1016/j.enconman.2006.09.011>.
- Coşkuner, G., 1994. Flow of sour gas, liquid sulfur, and water in porous media. *J. Colloid Interface Sci.* 165, 526–531. <https://doi.org/10.1006/jcis.1994.1259>.
- Culcer, D., Hu, X., Das Sarma, S., 2010. Interface roughness, valley-orbit coupling, and valley manipulation in quantum dots. *Phys. Rev. B* 82, 205315. <https://doi.org/10.1103/PhysRevB.82.205315>.
- Cygan, R.T., Greathouse, J.A., Kalinichev, A.G., 2021. Advances in clayff molecular simulation of layered and nanoporous materials and their aqueous interfaces. *J. Phys. Chem. C* 125, 17573–17589. <https://doi.org/10.1021/acs.jpcc.1c04600>.
- da Rocha, S.R., Johnston, K.P., Westacott, R.E., Rossky, P.J., 2001. Molecular structure of the water–supercritical CO<sub>2</sub> interface. *J. Phys. Chem. B* 105, 12092–12104. <https://doi.org/10.1021/jp12439z>.
- Das, A., Ali, S.M., 2019. Understanding of interfacial tension and interface thickness of liquid/liquid interface at a finite concentration of alkyl phosphate by molecular dynamics simulation. *J. Mol. Liq.* 277, 217–232. <https://doi.org/10.1016/j.molliq.2018.12.116>.
- Dehaghani, Y.H., Assareh, M., Feyzi, F., 2023. Molecular dynamics simulations study on equilibrium, transport, and interfacial properties of H<sub>2</sub>S-brine systems under conditions typical of geological sequestration. *Environ. Earth Sci.* 82. <https://doi.org/10.1007/s12665-023-11246-x>.
- Dong, X., Xu, W., Liu, H., Chen, Z., Lu, N., Wang, W., 2023. On the replacement behavior of CO<sub>2</sub> in nanopores of shale oil reservoirs: insights from wettability tests and molecular dynamics simulations. *Geoenergy Sci. Eng.* 223, 211528. <https://doi.org/10.1016/j.geoen.2023.211528>.
- Espeau, P., Céolin, R., 2007. Density of molten sulfur in the 334–508 K range. *Thermochim. Acta* 459, 127–129. <https://doi.org/10.1016/j.tca.2007.03.016>.
- Fan, C., Jia, J., Peng, B., Liang, Y., Li, J., Liu, S., 2020. Molecular dynamics study on CO<sub>2</sub> foam films with sodium dodecyl sulfate: effects of surfactant concentration, temperature, and pressure on the interfacial tension. *Energy Fuels* 34, 8562–8574. <https://doi.org/10.1021/acs.energyfuels.0c00965>.
- Fan, S., Wu, S., Lang, X., Wang, Y., Li, G., 2024. Insights of kaolinite surface and salt ions on the formation of carbon dioxide hydrates in confined nanopore: a molecular dynamics simulation study. *Gas Sci. Eng.* 129, 205390. <https://doi.org/10.1016/j.jgsce.2024.205390>.
- Fanelli, R., 1950. The surface tension of sulfur. *J. Am. Chem. Soc.* 72, 4016–4018. <https://doi.org/10.1021/ja01165a050>.
- Ferreira, A., Lobo, L., 2011. The low-pressure phase diagram of sulfur. *J. Chem. Therm.* 43, 95–104. <https://doi.org/10.1016/j.jct.2010.07.007>.
- Ghoufi, A., Malfreyt, P., 2018. Calculation of the surface tension of water: 40 years of molecular simulations. *Mol. Simul.* 45, 295–303. <https://doi.org/10.1080/08927022.2018.1513648>.
- Girifalco, L., Good, R.J., 1957. A theory for the estimation of surface and interfacial energies. I. Derivation and application to interfacial tension. *J. Phys. Chem.* 61, 904–909. <https://doi.org/10.1021/j150553a013>.
- Gong, Q., Wu, H., Yang, F., Tang, Z., 2023. Corrosion of pipeline steel weld metals containing alloying elements in CO<sub>2</sub>/H<sub>2</sub>S environment. *Gas Sci. Eng.* 109, 104846. <https://doi.org/10.1016/j.jngse.2022.104846>.
- González-Barramúo, B., Cea-Klapp, E., Polishuk, I., Quinteros-Lama, H., Piñeiro, M.M., Garrido, J.M., 2024. Molecular insights into the wettability and adsorption of acid gas-water mixture. *J. Phys. Chem. B* 128, 3764–3774. <https://doi.org/10.1021/acs.jpcb.4c00592>.
- Hayatizadeh, N., Chanzab, F.F., Falamaki, C., 2024. Adsorption of asphaltene molecules on functionalized SiO<sub>2</sub> nanoparticles at atmospheric and high pressures in heptane/toluene environment: a molecular dynamics simulation study. *Geoenergy Sci. Eng.* 234, 212684. <https://doi.org/10.1016/j.geoen.2024.212684>.
- Hess, B., 2002. Determining the shear viscosity of model liquids from molecular dynamics simulations. *J. Chem. Phys.* 116, 209–217. <https://doi.org/10.1063/1.1421362>.
- Huang, J., Zhai, C., Sun, Y., Lai, Y., Xu, H., Huang, T., Wang, Y., Li, Y., Xu, J., 2024. Microscopic scale influence of functional groups on the displacement behavior of

- coalbed methane by hot humid flue gas: a molecular simulation study based on the dynamic injection process. *Gas Sci. Eng.* 131, 205477. <https://doi.org/10.1016/j.jgsce.2024.205477>.
- Jones, R., Ballone, P., 2003. Density functional and Monte Carlo studies of sulfur. I. Structure and bonding in Sn rings and chains (n=2–18). *J. Chem. Phys.* 118, 9257–9265. <https://doi.org/10.1063/1.1568081>.
- Jorgensen, W.L., Maxwell, D.S., Tirado-Rives, J., 1996. Development and testing of the OPLS all-atom force field on conformational energetics and properties of organic liquids. *J. Am. Chem. Soc.* 118, 11225–11236. <https://doi.org/10.1021/ja9621760>.
- Kashefi, K., Pereira, L.M., Chapoy, A., Burgass, R., Tohidi, B., 2016. Measurement and modelling of interfacial tension in methane/water and methane/brine systems at reservoir conditions. *Fluid Phase Equilib.* 409, 301–311. <https://doi.org/10.1016/j.fluid.2015.09.050>.
- Kharazi, M., Saei, J., Torabi, M., Zolfogil, M.A., 2023. Molecular design and applications of a nanostructured green Tripodal surface active ionic liquid in enhanced oil recovery: interfacial tension reduction, wettability alteration, and emulsification. *Pet. Sci.* 20, 3530–3539. <https://doi.org/10.1016/j.petsci.2023.07.010>.
- Kotagodaheti, R., Hewage, K., Perera, P., Sadiq, R., 2023. Technology and policy options for decarbonizing the natural gas industry: a critical review. *Gas Sci. Eng.* 114, 204981. <https://doi.org/10.1016/j.jgsce.2023.204981>.
- Li, C., Liu, G., Peng, Y., 2018. Predicting sulfur solubility in hydrogen sulfide, carbon dioxide, and methane with an improved thermodynamic model. *RSC Adv.* 8, 16069–16081. <https://doi.org/10.1039/C8RA01744A>.
- Li, T., Ma, Y., Zeng, D., Zhang, R., Li, Q., Huang, L., 2024. Sulfur solubility in sour gas components and mixtures from a molecular perspective. *Fuel* 364. <https://doi.org/10.1016/j.fuel.2024.131047>.
- Li, X., Boek, E.S., Maitland, G.C., Trusler, J.M., 2012. Interfacial tension of (brines + CO<sub>2</sub>): CaCl<sub>2</sub> (aq), MgCl<sub>2</sub> (aq), and Na<sub>2</sub>SO<sub>4</sub> (aq) at temperatures between (343 and 423) K, pressures between (2 and 50) MPa, and molalities of (0.5 to 5) mol·kg<sup>-1</sup>. *J. Chem. Eng. Data* 57, 1369–1375. <https://doi.org/10.1021/je300304p>.
- Li, Z., Yao, J., Ren, Z., Sun, H., Zhang, L., Yang, Y., Fan, J., Kou, J., 2019. Accumulation behaviors of methane in the aqueous environment with organic matters. *Fuel* 236, 836–842. <https://doi.org/10.1016/j.fuel.2018.09.071>.
- Liu, W., Gao, B., Zhang, Z., Zhang, J., Zhang, D., Fan, M., Fu, X., Zheng, L., Liu, Q., 2010. H<sub>2</sub>S formation and enrichment mechanisms in medium to large scale natural gas fields (reservoirs) in the Sichuan Basin. *Petrol. Explor. Dev.* 37, 513–522. [https://doi.org/10.1016/S1876-3804\(10\)60051-1](https://doi.org/10.1016/S1876-3804(10)60051-1).
- Liu, Y., Li, H.A., Okuno, R., 2016. Measurements and modeling of interfacial tension for CO<sub>2</sub>/CH<sub>4</sub>/brine systems under reservoir conditions. *Ind. Eng. Chem. Res.* 55, 12358–12375. <https://doi.org/10.1021/acs.iecr.6b02446>.
- Liu, Y., Tang, J., Wang, M., Wang, Q., Tong, J., Zhao, J., Song, Y., 2017. Measurement of interfacial tension of CO<sub>2</sub> and NaCl aqueous solution over wide temperature, pressure, and salinity ranges. *J. Chem. Eng. Data* 62, 1036–1046. <https://doi.org/10.1021/acs.jced.6b00858>.
- Lu, T., Li, Z., Du, L., 2023. Enhanced CO<sub>2</sub> geological sequestration using silica aerogel nanofluid: experimental and molecular dynamics insights. *Chem. Eng. J.* 474, 145566. <https://doi.org/10.1016/j.cej.2023.145566>.
- Ludwig, R., Behler, J., Klink, B., Weinhold, F., 2002. Molecular composition of liquid sulfur. *Angew. Chem. Int. Ed.* 41, 3199–3202. [https://doi.org/10.1002/1521-3773\\_\(20020902\)41:17%3C3199::AID-ANIE3199%3E3.0.CO\\_2-9](https://doi.org/10.1002/1521-3773_(20020902)41:17%3C3199::AID-ANIE3199%3E3.0.CO_2-9).
- Ma, Y., Zhang, S., Guo, T., Zhu, G., Cai, X., Li, M., 2008. Petroleum geology of the Puguang sour gas field in the Sichuan Basin, SW China. *Mar. Petrol. Geol.* 25, 357–370. <https://doi.org/10.1016/j.marpetgeo.2008.01.010>.
- Mamatkulov, S.I., Rinne, K.F., Buchner, R., Netz, R.R., Bonthuis, D.J., 2018. Water-separated ion pairs cause the slow dielectric mode of magnesium sulfate solutions. *J. Chem. Phys.* 148. <https://doi.org/10.1063/1.5000385>.
- Matsushima, T., Ono, K., 1958. The interfacial tension between liquid sulfur and water. *Research Institute of Mineral Dressing and Metallurgy* 58–67.
- Meyer, B., 1976. Elemental sulfur. *Chem. Rev.* 76, 367–388. <https://doi.org/10.1021/cr60301a003>.
- Min, R.T., Negash, B.M., Jufar, S.R., Elryes, A.A.K., 2025. Screening of amino acids for enhanced CO<sub>2</sub> dissolution in saline aquifers: molecular dynamics simulation study. *Gas Sci. Eng.*, 205574 <https://doi.org/10.1016/j.jgsce.2025.205574>.
- Mutailipu, M., Liu, Y., Jiang, L., Zhang, Y., 2019. Measurement and estimation of CO<sub>2</sub>-brine interfacial tension and rock wettability under CO<sub>2</sub> sub- and super-critical conditions. *J. Colloid Interface Sci.* 534, 605–617. <https://doi.org/10.1016/j.jcis.2018.09.031>.
- Nath, S.K., 2003. Molecular simulation of vapor-liquid phase equilibria of hydrogen sulfide and its mixtures with alkanes. *J. Phys. Chem. B* 107, 9498–9504. <https://doi.org/10.1021/jp034140h>.
- National Institute of Standards and Technology, 2024. Thermophysical properties of Fluid Systems. <https://webbook.nist.gov/chemistry/fluid/>. (Accessed 20 June 2024).
- Ofori, K., Phan, C.M., Barifcanyi, A., Iglauer, S., 2023. Some interfacial properties of water and CO<sub>2</sub>/H<sub>2</sub>S at quasireservoir conditions: a molecular dynamics study. *SPE J.* 28, 783–795. <https://doi.org/10.2118/212843-PA>.
- Ono, K., Matsushima, T., 1957. The surface tension of liquid sulfur. *Research Institute of Mineral Dressing and Metallurgy*.
- Potoff, J.J., Siepmann, J.I., 2001. Vapor-liquid equilibria of mixtures containing alkanes, carbon dioxide, and nitrogen. *AIChE J* 47, 1676–1682. <https://doi.org/10.1002/aic.690470719>.
- Qian, C., Rui, Z.-H., Liu, Y.-L., Du, K., Liu, C., Zhao, Y., Ma, X.-M., 2024. Adsorption behavior of CO<sub>2</sub>/H<sub>2</sub>S mixtures in calcite slit nanopores for CO<sub>2</sub> storage: an insight from molecular perspective. *Pet. Sci.* <https://doi.org/10.1016/j.petsci.2024.03.016>.
- Rao, D.N., Lee, J.I., 2003. Determination of gas-oil miscibility conditions by interfacial tension measurements. *J. Colloid Interface Sci.* 262, 474–482. [https://doi.org/10.1016/S0021-9797\(03\)00175-9](https://doi.org/10.1016/S0021-9797(03)00175-9).
- Ren, Q., Chen, G., Yan, W., Guo, T., 2000. Interfacial tension of (CO<sub>2</sub> + CH<sub>4</sub>) + water from 298 K to 373 K and pressures up to 30 MPa. *J. Chem. Eng. Data* 45, 610–612. <https://doi.org/10.1021/je990301s>.
- Saraji, S., Piri, M., Goual, L., 2014. The effects of SO<sub>2</sub> contamination, brine salinity, pressure, and temperature on dynamic contact angles and interfacial tension of supercritical CO<sub>2</sub>/brine/quartz systems. *Int. J. Greenh. Gas Control* 28, 147–155. <https://doi.org/10.1016/j.ijggc.2014.06.024>.
- Shah, V., Broseta, D., Mouronval, G., Montel, F., 2008. Water/acid gas interfacial tensions and their impact on acid gas geological storage. *Int. J. Greenh. Gas Control* 2, 594–604. <https://doi.org/10.1016/j.ijggc.2008.02.002>.
- Steudel, R., Strauss, R., Koch, L., 1985. Quantitative HPLC analysis and thermodynamics of sulfur melts. *Angew. Chem. Int. Ed.* 24, 59–60. <https://doi.org/10.1002/anie.198500591>.
- Thompson, A.P., Aktulgä, H.M., Berger, R., Bolintineanu, D.S., Brown, W.M., Crozier, P. S., in't Veld, P.J., Kohlmeyer, A., Moore, S.G., Nguyen, T.D., 2022. LAMMPS-a flexible simulation tool for particle-based materials modeling at the atomic, meso, and continuum scales. *Comput. Phys. Commun.* 271, 108171. <https://doi.org/10.1016/j.cpc.2021.108171>.
- Vega, C., de Miguel, E., 2007. Surface tension of the most popular models of water by using the test-area simulation method. *J. Chem. Phys.* 126. <https://doi.org/10.1063/1.2715577>.
- Waldman, M., Hagler, A.T., 1993. New combining rules for rare gas van der Waals parameters. *J. Comput. Chem.* 14, 1077–1084. <https://doi.org/10.1002/jcc.540140909>.
- Wei, Y., Wang, L., Li, N., Wen, L., Huo, X., Zhang, L., Yang, M., 2022. Roles of carbon dioxide and methane in the dissolution of elemental sulfur in natural gas. *Energy Fuels* 36, 13617–13625. <https://doi.org/10.1021/acs.energyfuels.2c02968>.
- Wei, Y., Wang, L., Yang, Y., Wen, L., Huo, X., Zhang, L., Yang, M., 2023. Molecular mechanism in the solubility reduction of elemental sulfur in H<sub>2</sub>S/CH<sub>4</sub> mixtures: a molecular modeling study. *Fluid Phase Equilib.* 569. <https://doi.org/10.1016/j.fluid.2023.113764>.
- Werth, S., Horsch, M., Hasse, H., 2017. Molecular simulation of the surface tension of 33 multi-site models for real fluids. *J. Mol. Liq.* 235, 126–134. <https://doi.org/10.1016/j.molliq.2016.12.062>.
- Xia, X., Jiao, X., Li, J., Shen, W., Xia, Y., Wang, H., 2024. Gas adsorption behavior in shale reservoirs: insights from molecular scale. *Capillarity* 13, 68–72. <https://doi.org/10.46690/capi.2024.12.03>.
- Xu, F., Chen, Q., Ma, M., Wang, Y., Yu, F., Li, J., 2020. Displacement mechanism of polymeric surfactant in chemical cold flooding for heavy oil based on microscopic visualization experiments. *Adv. Geo-Energy Res.* 4. <https://doi.org/10.26804/ager.2020.0107>.
- Xu, J., Zhan, S., Wang, W., Su, Y., Wang, H., 2022. Molecular dynamics simulations of two-phase flow of n-alkanes with water in quartz nanopores. *Chem. Eng. J.* 430, 132800. <https://doi.org/10.1016/j.cej.2021.132800>.
- Yarveicy, H., 2023. Effect of nanoparticles on phase behavior of surfactant-oil-water system: an application in multiphase flow system. *Adv. Geo-Energy Res.* 9, 152–155. <https://doi.org/10.46690/ager.2023.09.03>.
- Yasuda, K., Mori, Y.H., Ohmura, R., 2016. Interfacial tension measurements in water-methane system at temperatures from 278.15 K to 298.15 K and pressures up to 10 MPa. *Fluid Phase Equilib.* 413, 170–175. <https://doi.org/10.1016/j.fluid.2015.10.006>.
- Yin, Y., Zheng, W., Lin, S., Zhao, L., 2023. Dissolution of forsterite surface in brine at CO<sub>2</sub> geo-storage conditions: insights from molecular dynamic simulations. *Langmuir* 39, 4304–4316. <https://doi.org/10.1021/acs.langmuir.2c03309>.
- Yuet, P.K., Blankschtein, D., 2010. Molecular dynamics simulation study of water surfaces: comparison of flexible water models. *J. Phys. Chem. B* 114, 13786–13795. <https://doi.org/10.1021/jp1067022>.
- Zeebe, R.E., 2011. On the molecular diffusion coefficients of dissolved CO<sub>2</sub>, HCO<sub>3</sub><sup>-</sup>, and CO<sub>3</sub><sup>2-</sup> and their dependence on isotopic mass. *Geochim. Cosmochim. Acta* 75, 2483–2498. <https://doi.org/10.1016/j.gca.2011.02.010>.
- Zhang, C., Wang, M., 2023. CO<sub>2</sub>/brine interfacial tension for geological CO<sub>2</sub> storage: a systematic review. *Geoenergy Sci. Eng.* 220. <https://doi.org/10.1016/j.jpetrol.2022.111154>.
- Zhang, D., Tang, H., Song, Y., Perera, M., Ranjith, P., 2024. Molecular simulation of the competitive adsorption of methane and carbon dioxide in the matrix and slit model of shale kerogen and the influence of water. *Geoenergy Sci. Eng.* 242, 213212. <https://doi.org/10.1016/j.jgeoen.2024.213212>.
- Zhang, J., Lei, D., Feng, W., 2014. An approach for estimating toxic releases of H<sub>2</sub>S-containing natural gas. *J. Hazard Mater.* 264, 350–362. <https://doi.org/10.1016/j.jhazmat.2013.09.070>.